GOCE derived vertical gravity gradient delineates great earthquake rupture zones along the Chilean margin

CrossMark

Orlando Álvarez [a,b,*], Silvina Nacif [a,c], Mario Gimenez [a,b], Andres Folguera [b,d], Carla Braitenberg [e]

[a] Instituto Geofísico y Sismológico Ing. Volponi, Universidad Nacional de San Juan, Ruta 12-Km17, San Juan, Argentina
[b] Consejo Nacional de Investigaciones Científicas y Técnicas, CONICET, Argentina
[c] Fondo Argentino Sectorial, Agencia de Promoción Científica y Tecnológica, FONARSEC, Argentina
[d] INDEAN - Instituto de Estudios Andinos "Don Pablo Groeber". Departamento de Cs. Geológicas - FCEN - Pab. II. Universidad de Buenos Aires, Argentina
[e] Department of Mathematics and Geosciences, University of Trieste, Via Weiss, I-34127 Trieste, Italy

ARTICLE INFO

ABSTRACT

In the south Central Andes region, the Nazca oceanic plate that subducts beneath the South American plate is characterized by a rough topography derived from different oceanic features that collide against the continental margin. These features determine an important segmentation of both the margin and of the interplate zone. The Chilean subduction margin has been characterized by megathrust earthquakes affecting the plate interface with large rupture areas reaching hundreds of kilometers parallel to the trench. The occurrence of these phenomena has been linked, among other causes, to the subduction of sediments that fill the trench and their spatial relation to the relatively prominent oceanic features. We calculated the topography corrected vertical gravity gradient from GOCE satellite data and from EGM2008 model in order to delineate mass heterogeneities related to density variations along the south-central Chile subduction zone. Obtained results show a spatial relation between the subduction of the Nazca oceanic highs and associated along-strike segmentation of the vertical gravity gradients over the interplate zone. We compared our results with the different rupture areas and found a good correspondence with the ellipses for the main earthquakes such as the Valdivia-1960 and Maule-2010 ones. Then, we compared vertical gravity gradients with slip distribution obtained from different models, finding that they are actually correlated with high slip over negative vertical gradient. The GOCE derived gradient adjusts better with the main slip distribution contour since its signal has a characteristic high wavelength. Instead, the EGM2008 model presents a better performance in defining the high frequency anomalies. However, the last results need to be considered only in those regions where the statistical comparison with GOCE data shows a good performance. This is because EGM2008 model data present varying quality of the original terrestrial data, while the quality of the GOCE data is locally homogeneous.

© 2014 Elsevier B.V. All rights reserved.

1. Introduction

Subduction zones are affected by the occurrence of giant earthquakes ($Mw \geq 8.0$) generally related to rupture zones (e.g. plate bounding faults) located in the contact between the underthrusting oceanic lithosphere and the overriding plate. The Chilean subduction zone has been the locus of giant earthquakes with rupture areas reaching hundreds of kilometers, widespread strong shaking, and destructive tsunamis (Ruff, 1989), e.g. the 1960 and 2010 earthquakes. Several studies related initially the age of the subducting oceanic lithosphere and relative convergence rate between plates with the variable seismic coupling and consequent earthquake size (Kanamori, 1971; Ruff and Kanamori, 1980; Uyeda and Kanamory, 1979). Recently, Heuret et al. (2011) explained that the subduction velocity is probably the first-order controlling parameter in physical characteristics of the plate interfaces, determining both the geometry and the mechanical behavior, finding an inverse relation between seismic coupling and subduction velocity.

Seismic coupling has also been related to the presence of excess trench sediments which enhances earthquake occurrence (Ruff, 1989). This author explained that excess in trench sediments could be associated with the subduction of a coherent sedimentary layer, which at elevated temperature and pressure forms a homogeneous and strong contact zone between the plates. Later, Lamb and Davis (2003) proposed additionally that these sediments could modify the transmission of tectonic stresses across the plate interface.

* Corresponding author at: Instituto Geofísico y Sismológico Ing. Volponi, Universidad Nacional de San Juan, Ruta 12-Km17, San Juan, Argentina. Tel.: +54 0264 4945015.
E-mail addresses: orlando_a_p@yahoo.com.ar (O. Álvarez), nacif.silvina@gmail.com (S. Nacif), gimmario@gmail.com (M. Gimenez), andresfolguera2@yahoo.com.ar (A. Folguera), berg@units.it (C. Braitenberg).

Moreover, the size and frequency of large earthquakes, according to some hypotheses, appear to be strongly influenced by subduction of highly buoyant oceanic features (*Hof's*) such as seamounts, fracture zones and seismic ridges (Bilek, 2007; Cloos, 1992; Cloos and Shreve, 1996; Das and Watts, 2009; Kelleher and McCann, 1976; Lay et al., 1982; Scholz and Small, 1997; Watts et al., 2010; among others). Subducting *Hof's* either may trigger earthquakes acting as seismic asperities (Bilek et al., 2003; Kanamori, 1994; Ruff, 1996) or may control the seismic moment release and rupture area acting as seismic barriers to earthquake rupture (Das and Aki, 1977; Kodaira et al., 2000; Wang and Bilek, 2011). This would depend on the degree of seismic coupling between the overriding and subducting plates in each region (Bilek, 2007). More recently, Contreras-Reyes and Carrizo (2011) proposed that high amounts of subducted sediments might smooth the subduction interface resulting in a homogenous coupled region allowing ruptures overcome these barriers. Such large and homogeneously coupled interface would favor along trench-parallel propagation of the rupture zone producing large earthquake magnitudes (Contreras-Reyes et al., 2010; Heuret et al., 2012; Ruff, 1989; Schertwath et al., 2009; among others).

Even though the role of bathymetric anomalies of the oceanic plate on seismogenic segmentation has been tested, based on direct bathymetric analysis (Contreras-Reyes and Carrizo, 2011; Müller and Landgrebe, 2012; Sparkes et al., 2010), this has been recognized as not the only cause for segmentation of megathrust at subduction zones. Recent works (Heuret et al., 2012; Scholl et al., 2010) have related empirically tectonic stresses and geometrical irregularities through the subduction interface to giant earthquakes. Analysis of the relationship between gravity field derivatives and seismogenic behavior at subduction zones has contributed stating that gravity anomalies allow observing lateral variations of density "hindered" below topography/bathymetry. These anomalies can then be connected with the geological structure of both plates and/or with the frictional structure of the interplate fault. Song and Simons (2003) had already correlated strong negative trench parallel gravity anomalies, in the area interposed between the coast and the trench, with maximum slip associated with large earthquakes. These authors had related negative gravity variations to high-shear traction on the interplate thrust, in association with an increase in the effective coefficient of friction (Llenos and Mc Guire, 2007). Wells et al. (2003) established a link between forearc gravity lows, active basins, enhanced subduction erosion and large coseismic slip, while Sobiesiak et al. (2007) observed positive correlations between seismic b-value, isostatic residual gravity anomalies and geologic structures along the Northern Chile margin. In this line, Tassara (2010) proposed that the correlation between gravity and seismogenic structure along the Chilean margin is mainly due to the heterogeneous density and geological structure of the upper plate forearc and its influence on spatially varying vertical stress loading the megathrust.

The study of the structure, geometry and segmentation along the interplate zone has been greatly enhanced by using potential methods. Gravimetry is very useful for this propose as it allows detecting mass inhomogeneities related to density variations. Particularly, satellite gravimetry that presents a regional and homogeneous coverage, and whose application to seismotectonic studies has not been a common practice, is been used in the present work. A new and complementary gravity derivative method, the vertical gravity gradient obtained from satellite data, allows delineating an anomalous mass with higher resolution than the gravity anomaly, especially where the density contrast is high (Alvarez et al., 2012; Braitenberg et al., 2011a). In this work, we use the vertical gravity gradient computed from GOCE satellite new data (Floberghagen et al., 2011; Pail et al., 2011) and from the EGM2008 model (Pavlis et al., 2008, 2012) to delineate mass heterogeneities along the Chilean subduction zone, with the aim of finding a potential relation with great rupture areas.

2. Tectonic setting and seismic segmentation

The western continental margin of South America, south of the Arica bend up to the triple point among the Nazca, Antarctica and South American plates, is characterized by the oblique subduction of the Nazca Plate beneath the South American margin (Fig. 1). The Peru–Chile trench, located at about 160 km off the coast, constitutes at surface the plate interface with approximately 5900 km in length and a mean width of 64 km (Lindquist et al., 2004; Völker et al., 2006).

In central Chile, at the latitudes of the subducted Nazca Plate (~33°S), the trench is segmented by the Juan Fernandez ridge (*JFR*), a hot spot chain formed by the amalgamation of a series of intraplate volcanoes interposed between the trench and ~900 km to the west (Yáñez et al., 2001), and to the south the Chile Rise, an active spreading center subducting at 46.5°S (Völker et al., 2006). Between the *JFR* and the Chile Rise numerous seamounts and fracture zones, relatively minor in terms of relief, are located, such as Mocha, Valdivia and Guafo transform systems (Fig. 1). These constitute oceanic highs that are progressively buried by trench sediments as they submerge beneath the frontal accretionary prism in the subduction zone (Völker et al., 2006).

The sedimentary infill within the trench is mostly sourced from the Andes and the fore-arc region and in a minor fraction from the abyssal Pacific plains (Lamb and Davis, 2003; Völker et al., 2006). The higher bathymetric gradients through the oceanic floor influence the distribution of sediments along the trench (Ranero et al., 2006). Within this trench, a north-flowing axial channel that extends north of 42°S for some 1000 km terminating at *JFR*, channels turbidity currents (Völker et al., 2006). Then the *JFR* ridge constitutes a topographic barrier within the trench that restrains the northward transport of these sediments along the trench (Yáñez et al., 2001; among others). Therefore, north of 32.5°S the trench is either completely starved or contains less than 1 km of sediments in thickness, being confined to a narrow axial zone (Bangs and Cande, 1997; Schweller et al., 1981; among others). South of the *JFR* up to the Chile Triple Junction, the trench is partly to completely filled, mainly by turbiditic sections determining a flat bottom bathymetry (Lamb and Davis, 2003; Ranero et al., 2006; Völker et al., 2006). Along this section, sediment thickness varies from 2,2 km to 3,5 km, in accordance with an increment in trench width from 25 km (33°S) to 80 km (41°S) (Völker et al., 2006). Variable volume of sediments along the trench, and its relation to the incoming subducting *Hof's*, strongly affects the development of the subduction channel and promotes seismic segmentation (Contreras-Reyes and Carrizo, 2011; Kopp, 2013).

Sparkes et al. (2010) found that rupturing in great earthquakes is likely to be impeded by subducted topography with positive relief (>1000 m), after analyzing the rupture limits of thirteen historic large earthquakes along the South America–Nazca plate interface. In this line, Contreras-Reyes and Carrizo (2011) studied the spatial relationship between large underthrusting earthquakes (Mw ≥ 7.5) and bathymetric heterogeneities along the Chile–Peru subduction zone, finding a strong relation between subduction of *Hof's* and earthquake rupture segments. More precisely, Müller and Landgrebe (2012) found a statistical relation between large earthquakes and the subduction of oceanic fracture zones at a global scale, and also explained that other oceanic features such as aseismic ridges and seamounts present an aseismic behavior. This is supported by previous works which pointed out that subduction of shallow seafloor relief produces crustal erosion inhibiting the accumulation of elastic strain energy creating weak, aseismic zones at the plate interface. This promotes an unfavorable condition for the generation and propagation of large ruptures (Mochizuki et al., 2008; Singh et al., 2011; Sparkes et al., 2010; Wang and Bilek, 2011).

Major rupture zones exemplify these relations. The Maule 2010 earthquake ruptured bilaterally through two major slip patches (Delouis et al., 2010; Lay et al., 2010; Lorito et al., 2011; Moreno et al.,
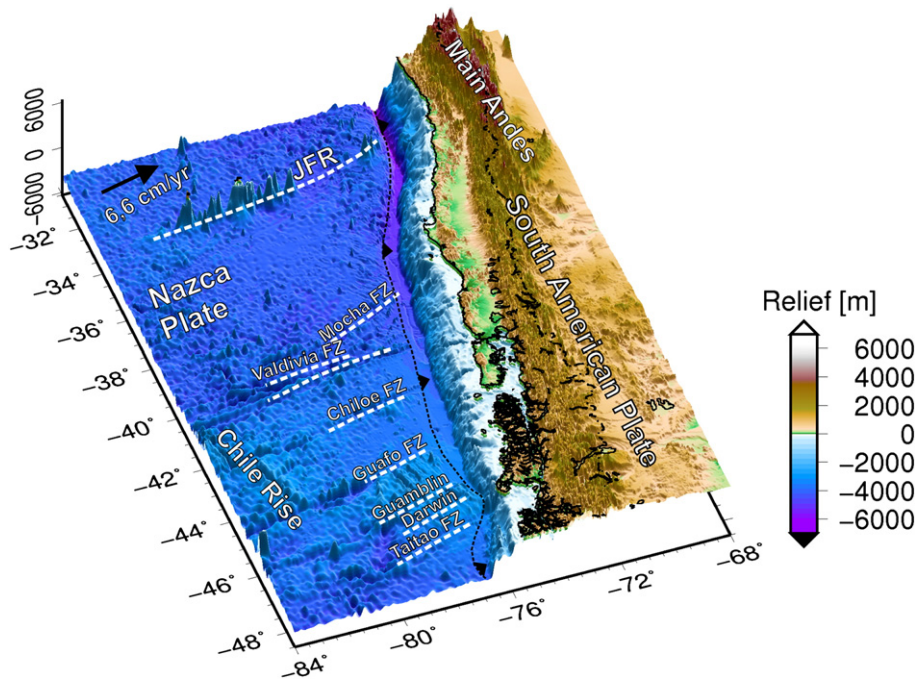
Fig. 1. Morphology of the oceanic Nazca plate highlighting the main topographical features that are subducted at the Chilean trench (Amante and Eakins, 2009). Note the differences in sediment thickness north and south of the Mocha Fz, and the JFR. Nazca/South America convergence rate is approximately 6.6 cm/yr with a convergence angle of 78°N (DeMets et al., 2010; Kendrick et al., 2003). Chilean/Argentinian border is indicated by dotted and dashed line; coast line by black line; dotted line indicates Chilean trench.

2012; Pollitz et al., 2011; Tong et al., 2010; Vigny et al., 2011), coinciding approximately the northern patch (Fig. 2) with the most probably 1928 rupture zone, abutting to the north against the rupture area of the 1985 event (Lange et al., 2012). The northern end of the rupture zone for the last event is located near the subducted JFR at the Chilean trench (~32.5°S). The 2010 Maule aftershocks and the coseismic slip ended to the south at the entering Mocha Fz, where the major asperity of the 1960 earthquake sequence is thought to have occurred (Lange et al., 2012; Lorito et al., 2011). The rupture zone of the 1960 earthquake ranges from the Mocha Fz to the Chile Rise, where slip distribution also appears to be segmented by the incoming *Hof's* (Contreras-Reyes and Carrizo, 2011; Melnick et al., 2009; Moreno et al., 2009).

3. Data and methods

The study of crustal anomalies at regional scale using gravity data has been enhanced by the new earth gravity field models, with increasingly improved resolution and accuracy from the new satellite missions (e.g. EGM2008 model from Pavlis et al., 2008, and GOCE models from Floberghagen et al., 2011; Pail et al., 2011; among others). Regional structures, suture zones and partially buried volcanic Provinces have been delineated by different studies by means of these models (e.g. Alvarez et al., 2012, 2014; Braitenberg, in press; Braitenberg et al., 2011a; Eyike et al., 2010; Li et al., 2013; Mariani et al., 2013; among others).

The satellite GOCE mission (Gravity Field and Steady-State Ocean Circulation Explorer, 2009–2013) was the most recent mission from the European Space Agency designed to obtain global and regional models of the gravity field and geoid with unprecedented high resolution and accuracy. Two techniques were utilized to fulfill these objectives: the gradiometry (whose main instrument, an electrostatic gravity gradiometer (EGG) measures the rate of change of the gravity vector in all three perpendicular directions) and the satellite-to-satellite tracking in a high-low mode (SST-hl, a double frequency GPS receptor is used to extract gravimetric information by means of an accurate orbit perturbation analysis). By combining these techniques, it is possible to recover the underlying dynamic models that govern the satellite motion, including the earth gravity field.

The earth gravity field models are given as a series of spherical harmonic coefficients up to a maximum degree/order on which depends the spatial resolution of the model (Barthelmes, 2009). The last models obtained from pure satellite GOCE data (e.g. GO_CONS_GCF_2_TIM_R4, http://icgem.gfz-potsdam.de/ICGEM/, Pail et al., 2011) are developed up to degree/order N = 250, so the smallest resolvable feature of the gravity field is equal to $\lambda/2 = 80$ km. Since the gravity field attenuates at the high altitude of satellites orbits, these models (satellite only) provide information only on the long wavelength part of the spectrum (Reguzzoni and Sampietro, 2010). Despite this disadvantage, GOCE derived models, have homogeneous precision, as no errors or sampling biases, induced by the terrestrial data, are present, as is the model EGM2008 (a spatially heterogeneous combination of data).

Particularly, the Time Wise Model solution (TIM) is a GOCE-only solution (GOCE orbits and gravity gradients) in a rigorous sense, as no external gravity field information is used (neither as reference model, nor for constraining the solution). The TIM_R4 model has the advantage of longer data span than previous GOCE based models and improved gradiometer data based on the Level-1 data processing strategy given by Stummer et al. (2012). The TIM models have been externally validated by independent GPS/leveling observations for Germany (875 stations) and Japan (873). Results (e.g. Hirt et al., 2011, 2012) indicate that globally the pure GOCE-model TIM_R4 performs significantly better than EGM2008; even though the latter contains also terrestrial gravity data (see GO_CONS_GCF_2_TIM_R4 datasheet from http://icgem.gfz-potsdam.de/ICGEM/).

The global earth gravity field model EGM2008 (Pavlis et al., 2008, 2012) that combines different kind of data presents the higher currently available spatial resolution (N = 2159 / $\lambda/2 = 9$ km) but when compared (up to the same degree/order) with the GOCE model, exhibits some differences (see Appendix A). EGM2008 is a combined solution composed of a worldwide surface gravity anomaly database of $5' \times 5'$
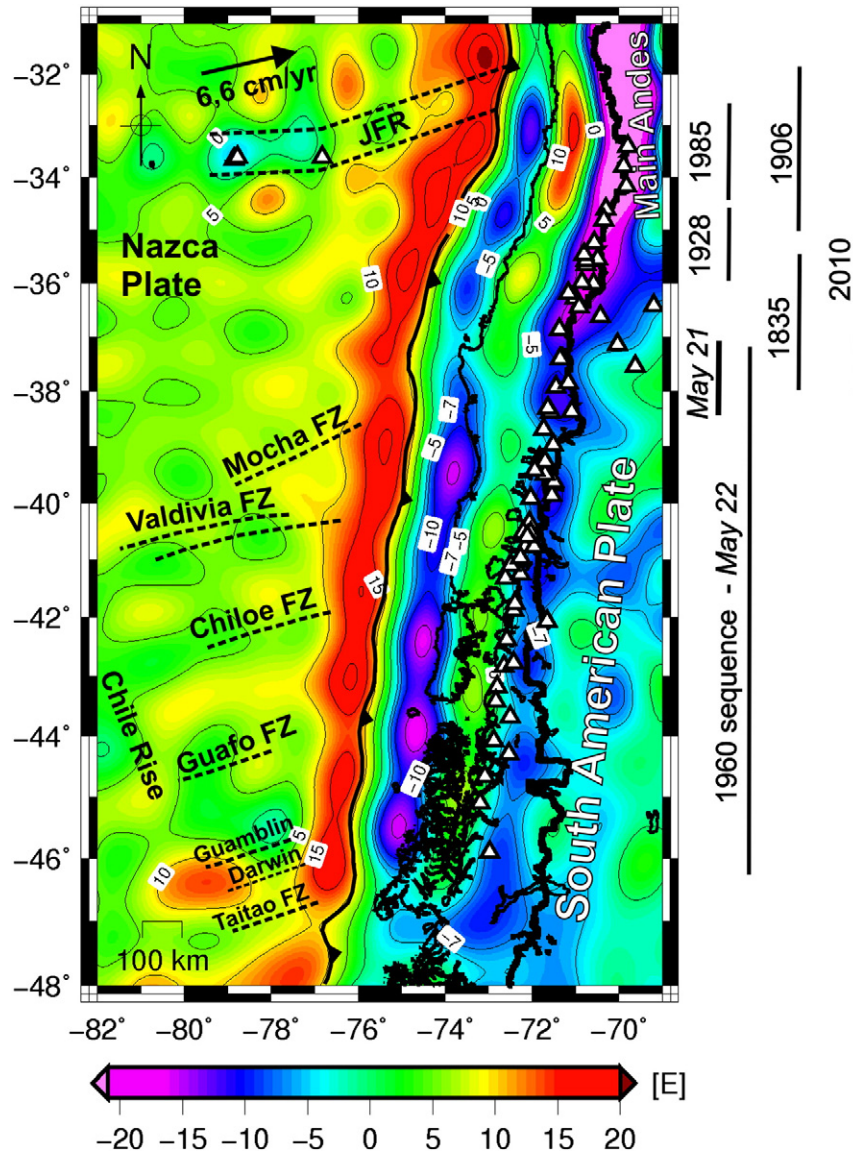
Fig. 2. Topography corrected Vertical Gravity Gradient (Tzz) obtained from GOCE (Pail et al., 2011) and Nazca plate *Hof's* (dashed lines). To the right the dimensions of the approximate rupture areas of the largest earthquakes along the Chile margin are indicated: **Valparaíso-1985, Mw = 8.0**: Barrientos (1988, 1995); Mendoza et al. (1994). **Valparaíso-1906, M$_s$ = 8.4**: Beck et al. (1998). **Talca-1928, Ms = 8.0**: Beck et al. (1998); Campos et al. (2002); Ruegg et al. (2009). **1835 Concepción-Constitución seismic gap, Mw = 8.5**: Campos et al. (2002); Darwin (1840, 1876); FitzRoy (1839); McCann et al. (1979). **Maule-2010, Mw = 8.8**: Lay et al. (2010); Lorito et al. (2011); Moreno et al. (2012); Vigny et al. (2011); among others. **Concepción May 21–1960, Mw = 8.2**: Cifuentes (1989); Engdahl and Villasenor (2002); Plafker and Savage (1970). **Valdivia May 22–1960, Mw = 9.5**: Moreno et al. (2009); Plafker and Savage (1970); Ruegg et al. (2009). Triangles indicate the current position of the active volcanic arc (Siebert and Simkin, 2002). Coastal line: thin black line, National borders: thick black line.

resolution (derived from terrestrial gravimetry, satellite altimetry, ship-borne and airborne gravimetry), and GRACE-derived satellite solutions (ITG-GRACE03S, Mayer-Gürr, 2007). Over poorly covered regions (areas where only lower resolution gravity data were available), their spectral content was "filled-in" with the computation of Topographic/Isostatic gravitational models (i.e. information implied by the topography; Pavlis et al., 2012). Over these areas, the gravity anomaly information over the harmonics of degree from 721 to 2159 is supplemented by the gravitational information obtained from the analysis of a global set of Residual Terrain Model-Implied (RTM-Implied) gravity anomalies.

The accuracy of the terrestrial gravity observations depends on the precision of the height measurements, so important inconsistencies arise when considering large areas; the sparseness of data in some large continental regions does not allow for the recovery of low frequencies of the gravimetric signal (Reguzzoni and Sampietro, 2010). Braitenberg et al. (2011b) and Bomfim et al. (2013) showed in detail how errors at high degree, enter the error of a downscaled EGM2008. The agreement between EGM2008 and the GOCE models is good where high quality terrestrial mean gravity anomalies are available, such as in North America, Europe and Australia (geoid RMS-differences on the order of 4–6 cm), although where the surface gravity data available for the development of EGM2008 is poor (South America, Africa, South-East Asia or China), the RMS-differences span between 20 and 38 cm (Yi and Rummel, 2014). When analyzing the areas of the various EGM2008 data sources, the "filled-in" regions present high RMS-geoid height differences, and here GOCE data lead to a significant improvement (Yi and Rummel, 2014). Summarizing, the gravity derivatives obtained

from GOCE model (Pail et al., 2011), allows delineating gravity anomalies at a regional scale (tectonic interpretation of medium to long wavelengths) with higher precision but with lower resolution than the EGM2008 model.

After the statistical analysis (Appendix A) and considering the sparseness of terrestrial data in the region under study (Pavlis et al., 2008, 2012), the most reliable areas to apply the EGM2008 model are mainly off-shore and forearc regions comprised between 36°S and 40°S (Figs. A.1 and A.3, Appendix A). Thus the GOCE model (TIM_R4) is more appropriate to apply than the EGM2008 model in the region under study despite its lower resolution (but with a homogeneous precision). Results obtained by means of the EGM2008 model will only be analyzed and compared to GOCE in the regions of higher performance, in order to solve the different anomalies in greater detail. The combined use of both models, considering their best individual qualities, has been tested in different studies (Alvarez et al., 2012, 2014). Köther et al. (2012) explained that combined gravity models (as EGM2008) can be used for density modeling of relatively smaller features such as shallower crustal structures, while satellite-only models are not appropriate for this "higher detail" purpose due to their low spatial resolution.

3.1. The vertical gravity gradient

From the earth gravity field models, the disturbing potential T is calculated. Then different derived quantities can be obtained such as the gravity anomaly and the gravity gradient tensor (TGG). The TGG or Marussi tensor is composed of five independent elements and is obtained as the second derivative of the anomalous potential (Hofmann-Wellenhof and Moritz, 2006). The Marussi tensor components $\underline{M} = (T_{ij})$ can be expressed and solved numerically in a spherical coordinate system (Rummel et al., 2011; Tscherning, 1976). The vertical gravity gradient (Tzz) is the second derivative of the disturbing potential in the radial direction:

$$T_{zz} = \frac{\partial^2 T}{\partial r^2} \left[1\ Eötvös = 10^{-4}\ \frac{mGal}{m} \right]$$

where T[r, φ, λ] is the anomalous potential, r the radial distance, and φ, λ the latitude and longitude respectively.

The vertical gravity gradient highlights superficial density anomalies and allows delineating the location of an anomalous mass with better detail and accuracy than the gravity anomaly itself (Braitenberg et al., 2011a). The Tzz presents a better theoretical resolution than the gravity vector for some geophysical features (Li, 2001). Since the Tzz is a derivative of gravity, the spectral power of gravity gradient signals is pushed to higher frequencies, resulting in a signal more focalized to the source than the gravity anomaly. Conversely, the latter has more signal power at low frequency making it more sensitive to regional signals and deeper sources.

The Tzz is more sensitive to superficial density variations relative to gravity and is totally insensitive to flat extended mass inhomogeneities, whereas a flat mass sums to the superficial effect of the gravity. Therefore Tzz is better for detection of the edge of geological structures and to distinguish the signal due to a smaller superficial density variation from an extensive deeper mass (Alvarez et al., 2012). In the area under study, between the trench and the coast line the sediment infill determines with the ocean floor a flat bottom topography, impeding to detect density differences by means of the Ga, which emphasizes the use of Tzz. This results in an improvement in outlining shallow buried structures when compared to Free Air or Bouguer gravity anomalies. A positive gradient value is related to denser bodies while a negative value is related to less dense bodies, and abrupt changes may indicate a high density contrast between two different lithologies.

3.2. Calculation

In order to delineate the spatial distribution of the anomalies related to density variations along the Chilean margin we calculated the vertical gravity gradient (Tzz) field from the model expressed as coefficients in a spherical harmonic expansion (Janak and Sprlak, 2006). For calculation we used the global model of GOCE GO_CONS_GCF_2_TIM_R4; Pail et al., 2011) in a geocentric spherical coordinate system at the calculation height of 7000 m to ensure that all values were above the topography. The values were calculated on a regular grid with a cell size of 0.05°, with the maximum degree and order of the harmonic expansion (N = 250) for this model. The topographic effect was removed from the fields in order to eliminate the correlation with the topography (Alvarez et al., 2013). Topographic mass elements obtained from the global relief model ETOPO1, which include ocean bathymetry (Amante and Eakins, 2009), were approximated with spherical prisms (Grombein et al., 2010, 2013; among others) of constant density in a spherical coordinate system to take into account the Earth's curvature (Uieda et al., 2010). Calculation with spherical prisms is needed since a planar approximation induces a considerable error (Bouman et al., 2013; Grombein et al., 2010, 2013). Differences between calculations using spherical and rectangular prisms are shown in Alvarez et al. (2012), Heck and Seitz (2007), Wild-Pfeiffer (2008), among others. A standard density of 2.67 g/cm^3 was used for masses above sea level and a density of 1.03 g/cm^3 for the sea water. The topographic correction amounts up to tens of Eötvös for the Tzz. It becomes higher over the maximum topographic elevations (e.g. the Main Andes) and lower over the topographic depressions such as the Chilean trench.

4. Results

The vertical gravity gradient (Tzz) highlights the mass inhomogeneities of the Nazca oceanic plate, the paths of the Juan Fernandez Ridge (JFR), and the Chile Rise being notorious both expressed by gradient values lower than in the surrounding bathymetry (Fig. 2). Seaward of the trench, the outer rise of the downgoing Nazca plate is marked by a high positive Tzz, indicative of a shallower asthenosphere related to the bending of the oceanic plate prior to subduction. This is segmented by the different oceanic plate features (Hof's), being particularly notorious the inception of the JFR, the Mocha Fz and the Chile Rise in the trench.

The abrupt decrease in the gradient signal east to the trench is due to the effect of the low density trench sediment infill which is accreted and underthrusted in the accretionary prism and subduction channel respectively. Between the trench and the coastline, an elongated trench parallel negative Tzz anomaly is noted, reaching less than −10 Eötvös. This low gradient signal is dominated by the effect of low-density sediment filling marginal sections and a thinner crust beneath the forearc deep sea terrace. Sediment filled slope basins, resting upon thinned continental crust that extends to about 50 km of the trench, were recognized in free-air gravity maps and in seismic profiles of the southern Chile margin (ANCORP Working Group, 2003; Flueh et al., 1998; von Huene et al., 1997). Wells et al. (2003) found prominent free-air gravity lows following the physiographic slope and basins in areas of high sedimentation rate as the Southern Chile continental margin. The JFR marks the northern termination of this low Tzz, while the Chile Rise and the Mocha Fz mark important attenuations.

As indicated, the crest of the subducted JFR causes uplift of the trench and forearc topography, blocking axial sediment transport in the trench (Kopp, 2013; Laursen et al., 2002; von Huene et al., 1997). The more positive values of Tzz north of JFR represent the scarcity of sediment infill into the trench at these latitudes. Here, Bangs and Cande (1997) reported a narrow sedimentary prism (<1.0 km) that passes to a starved trench north of Copiapo (27°S). The Tzz evinces these trench sediment thickness variations showing very low values south of JFR, intermediate
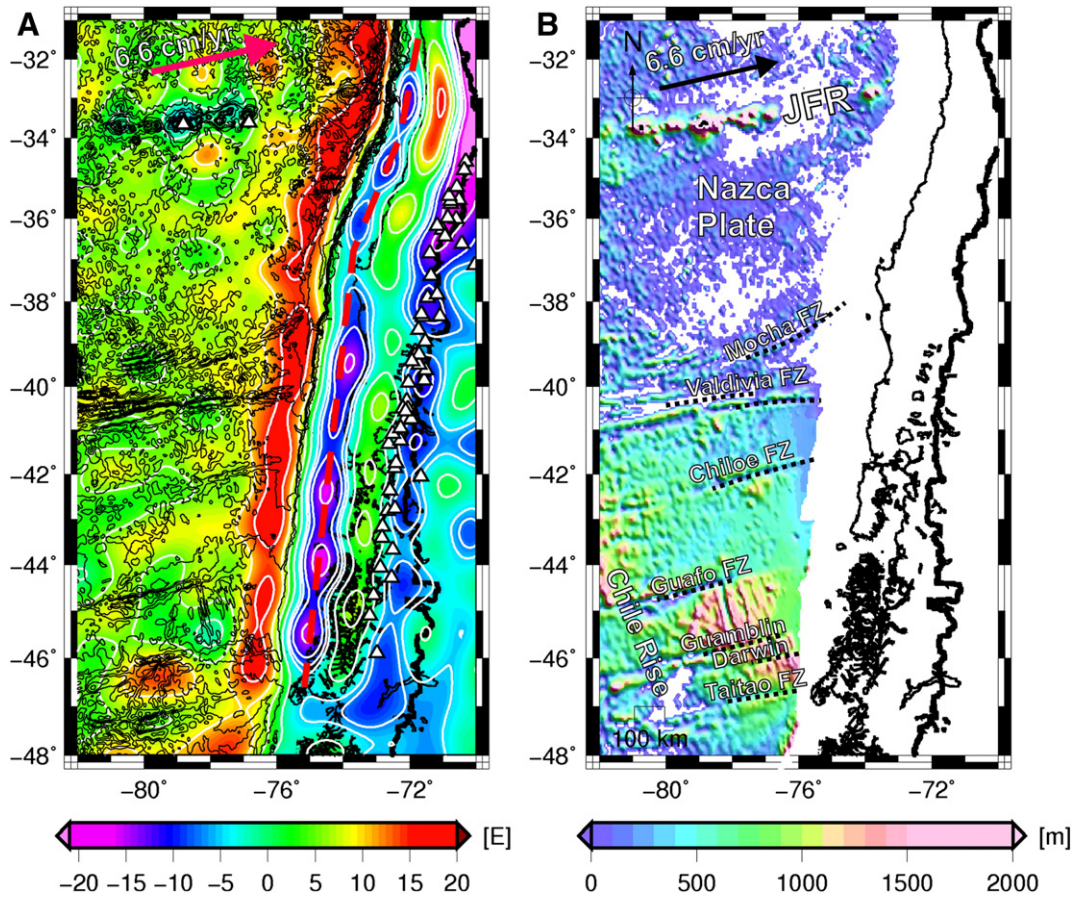
Fig. 3. (A): Relation between the variable relief of the oceanic floor and the segmentation of the Tzz signal. Black contours delineate bathymetry, while white contours show the Tzz segmentation. Red arrow indicates the convergence direction between Nazca and South American plates. Red dashed line shows the Tzz profile location of Fig. 4. (B): Positive relief of the oceanic Nazca plate relative to the mean seafloor depth of approximately −4000 m.
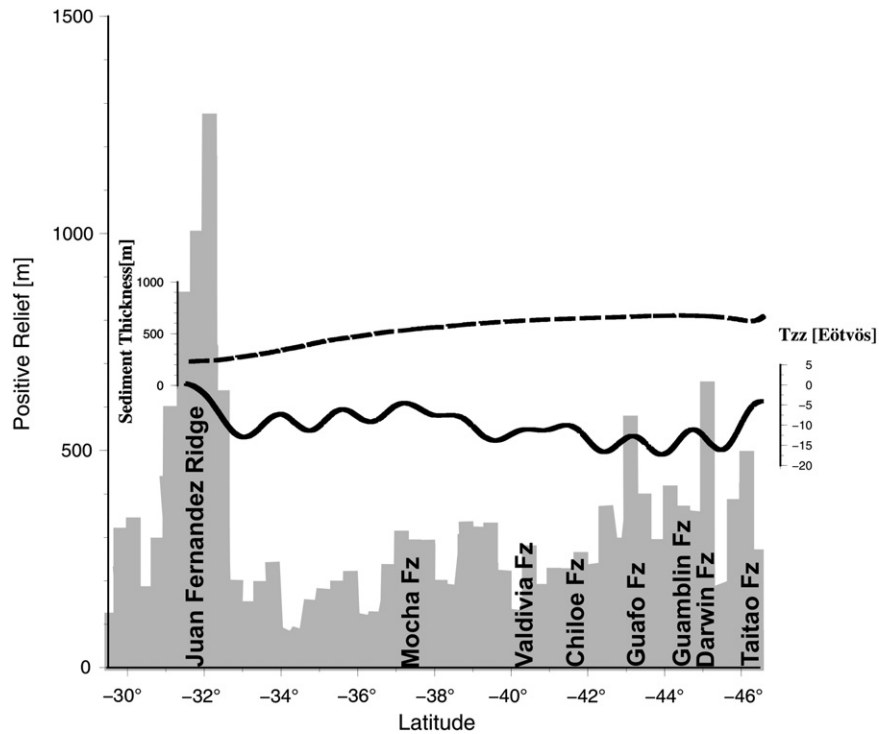

Fig. 4. Latitudinal cross section of the inferred subducted seafloor relief through the Nazca plate beneath the accretionary prism (gray shaded). Superimposed is the Tzz signal (black line). Note the general correlation that exists between bathymetry and Tzz. The observed little shift is a consequence of the obliquity between bathymetry profiles and Tzz (see Fig. 3) related to the convergence direction and because the Tzz signal has a long wavelength characteristic. Black dashed line delineates the sediment thickness from Whittaker et al. (2013).

values between *JFR* and the Copiapo ridge and positive values north of it (Figs. 2 and E.1 in Appendix E).

At the Chile Rise (46.5°S), the subduction of the spreading center promoted the swallowing of the trench bathymetry (Fig. 1) with the subsequent abrupt decrease in the sediment thickness (Bangs and Cande, 1997), and the narrowing of the frontal accretionary prism (Cande et al., 1987). These features are revealed by a higher *Tzz* signal at these latitudes (46.5–47°S). The positive *Tzz* that parallels the coastline along the forearc is the expression of high density materials, probably related to obducted Permo-Triassic fragments of offscraped oceanic crust engulfed in the active accretionary prism, typical of most convergent margins (Hackney et al., 2006).

The negative gradient signal that parallels the trench is divided into a series of segments by zones of higher *Tzz* values. Such segmentation is probably related to the depth variation of the subducted oceanic crust since higher *Tzz* values coincide with the entering *Hof's* (Figs. 3 and 4). These highs in the *Tzz* signal may also be related to denser intruded bodies offscraped into the accretionary prism. Spatial variation of the *Tzz* signal, therefore reveals the location of mass heterogeneities of the upper crust over the seismogenic zone. South of Mocha Fz, lower *Tzz* mean values over the seismogenic zone were obtained, reaching less than − 15 Eötvös (magenta elliptical anomalies of Fig. 2, see also profile of Fig. 4). Between Mocha Fz and the Chile Triple junction, sediment thickness is higher to the south, in relation with a thicker subduction channel (>1.5 km) (Contreras-Reyes and Carrizo, 2011). North of it, between *JFR* and Mocha Fz the subduction channel is only < 1.0 km thick. These authors indicate that this contrasting thickness has a strong influence in rupture propagation size. Whereas north of the Mocha Fz, the *Hof's* mainly control the size of the rupture area, to the south the thick subduction channel has a stronger influence on the abnormally large rupture propagation areas that affected the region. In fact, Heuret et al. (2011) reported a higher seismic coupling in this region south of Mocha Fz, where lower *Tzz* mean values are found over the seismogenic zone.

4.1. Relation between Hof's and segmentation along trench parallel Tzz signal

In this section, we explore the relation between the variable relief of the segmented oceanic floor and the segmentation of the *Tzz* signal along the seismogenic zone, as it is a good indicator of density heterogeneities. In the next section (4.2) we compare results of the *Tzz* signal with large earthquake rupture zones.

We contoured the relief from ETOPO1 (Amante and Eakins, 2009) at 500 m intervals and then superimposed to the topography corrected vertical gravity gradient from GOCE (Fig. 3A). A notorious relation between these bathymetric irregularities and *Tzz* highs/lows comes out from this analysis. It is noted that the oceanic relief contours (black contours of Fig. 3A) projected into the subduction zone following the convergence direction, roughly coincide with the *Tzz* segmentation over the seismogenic zone (white contours of Fig. 3A).

In order to highlight this relation, we have recalculated seafloor bathymetry by taking the difference between the depth at a point and the mean depth of the seafloor, taken as approximately − 4000 m (Sparkes et al., 2010) using seafloor topography from ETOPO1 (Amante and Eakins, 2009). Data were selected about 100 km away from the trench (Fig. 3b), since fracture zone topography is often completely covered by sediments close to the trench and in order to avoid the forebulge high zone (Franke et al., 2008; Müller and Landgrebe, 2012; Robinson, 2007). Then we calculated block mean values from the seafloor relief on sliding windows of 20′ × 20′. The mean values were extrapolated to the east into the subduction zone following the relative convergence between the Nazca and South American plates (Fig. 4). In this step, we assumed a continuity of the seamount chain beneath the continent with a relief of similar in magnitude to the present seafloor topography next to the plate interface as assumed by Sparkes et al. (2010).

Additionally, a profile following the minimum *Tzz* signal was traced (see Fig. 3A for profile location).

Three regional maxima of the *Tzz* signal (Fig. 4) are related to the *JFR*, the Mocha Fz and the subduction of the Chile Rise (at Taitao Fz). Between the *JFR* and the Mocha Fz the high/low values of the *Tzz* signal are related to high/low's of the inferred subducted seafloor. The region of the inferred location of the subducted Mocha Fz presents a smoothed *Tzz* signal, probably related to a wider zone of deformation resulting from the obliquity of this Fz with respect to the convergence angle and to the trench (based on a pure geometric analysis — Japas and Re (2005)). To the south of Valdivia Fz, a similar pattern to the one observed north of Mocha Fz is found (Fig. 4). Here, the bathymetric high/lows related to the different fracture zones also appear to be related to the high/low values of *Tzz* across the interplate zone. This is always considering that the GOCE model has a long wavelength character and thus smoothes the anomalies impeding an exact matching with the inferred subducted bathymetric anomalies.

4.2. Relation between Tzz and seismic segmentation

Wells et al. (2003) found that there is a tendency for coseismic slip in subduction faulting to be focused beneath the forearc basins and deepsea terrace gravity low, rather than beneath the intervening highs, based on a gravimetric analysis. They indicate that this could reflect along-strike variations in the temperature, fluid pressures, and stresses on the subduction zone caused by variations in overlying crustal thickness and density. If coseismic slip tends to be concentrated beneath these low density materials, and since the *Tzz* highlights mass inhomogeneities, this could be a good indirect indicator of the seismogenic structure.

In order to find a spatial correlation between the *Tzz* anomalies and large earthquake rupture zones along the Chilean margin, the extent of the inferred rupture areas were plotted (Fig. 2). Sparkes et al. (2010) indicate that there is a degree of uncertainty (less than 50 km, Kelleher, 1972) in the mapped limits of rupture zones that is due to different factors such as the gradual decrease in slip toward the rupture tip, the imperfect correlation between the rupture zone and the distribution of aftershocks, seismic intensities and co-seismic subsidence. In spite of this, the mapped rupture areas were compared to *Tzz* segmentation as a first approach.

In particular, the rupture areas that correspond to the 1985, 1928 and 1835 earthquakes roughly coincide with one *Tzz* patch of about − 7 Eötvös (Fig. 2, from north to south respectively). The positive anomaly above + 10 Eötvös, observed at the forearc, probably reveals the location of a seismic barrier marking the eastern edge of the rupture propagation zone for 1906 and 1985 events. The main rupture zone for the Maule 2010 earthquake embraces two low *Tzz* anomalies, being limited to the south by the entering Mocha Fz at its intersection point with the trench. The northern *Tzz* anomaly is more pronounced (more negative) than the southern one, and approximately coincides with the 1928 rupture zone, and also with the northern stronger, in terms of displacement, patch of the 2010 earthquake. The northern ending of the Maule 2010 and 1928 main rupture zones coincide with the southern ending of the rupture of the 1985 earthquake. At this latitude (34°S) the − 10 Eötvös contour narrows and throttles, indicating a discontinuity in the *Tzz* signal, probably influenced by the existence of a barrier (Figs. 4 and 5).

The large Valdivia 1960 earthquake rupture zone ends, to the north, at the southern termination of the 2010 rupture and develops to the south up to the Chile rise (47°S). Contreras-Reyes and Carrizo (2011) propose that the Mocha Fz has an important role in controlling the rupture propagation area of the 1960 and 2010 earthquakes. The northern and southern limits for the 1960 earthquake rupture, coincide with a notorious narrowing in the *Tzz* contours. The Concepcion earthquake in May 21–1960, Mw 8.2 earthquake (Fig. 2) occurred one day before the Valdivia earthquake Mw 9.5 (Ruiz et al., 2012). Its rupture area is
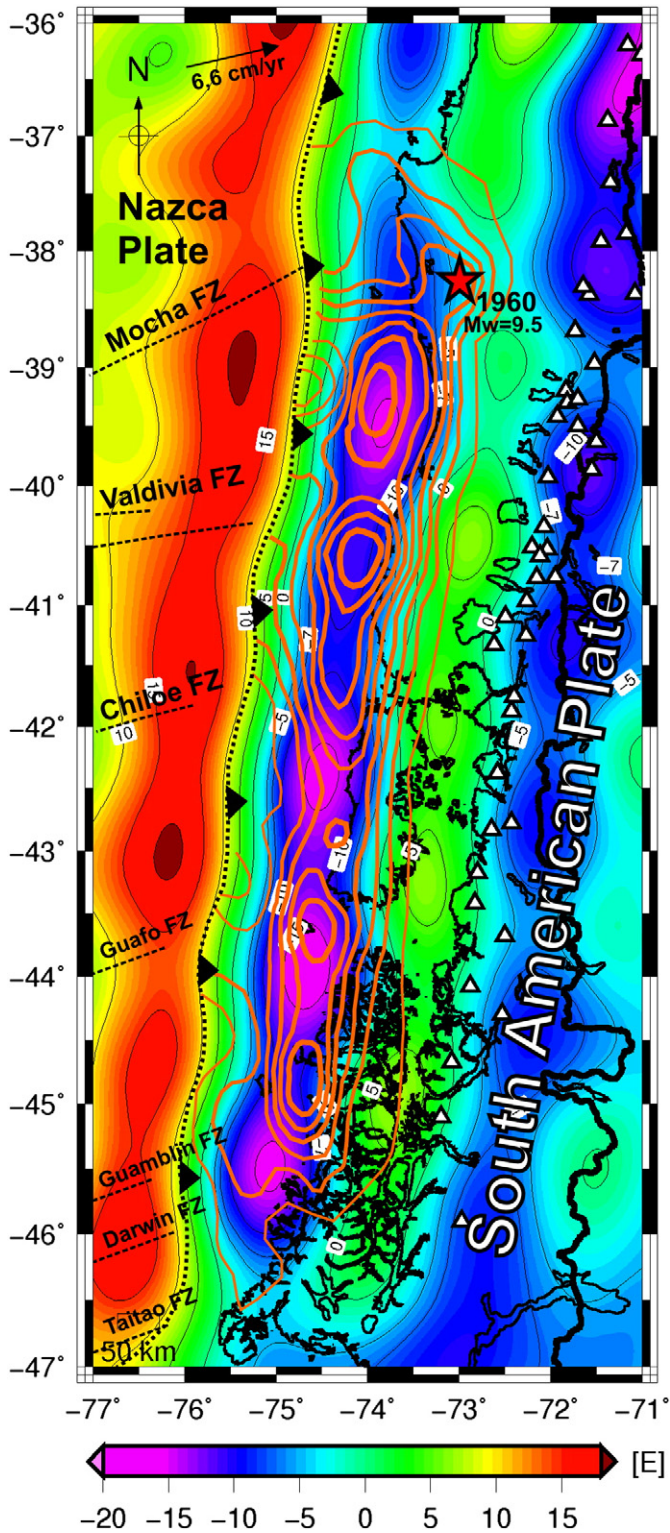
Fig. 5. Fault slip distribution contours predicted by the precise 3D FEM model of Moreno et al. (2009) superimposed to GOCE Vertical Gravity Gradient in the zone of the Valdivia 1960 earthquake. The northern −10 Eötvös contour coincides with slip distribution pattern. South of 42°S the correspondence is not so clear, showing a shift between the Tzz lows and the slip model. As mentioned in the text, Moreno et al. (2009) reported that south of Isla de Chiloé (42°S) data used for the inversion are not as reliable as in the northern zone.

comprised in the area of wide deformation related to the Mocha Fz coinciding with a smooth Tzz. Contrastingly, the Valdivia May 22–1960 main slip is comprised between two inferred subducted bathymetric highs (Mocha Fz and Chiloé Fz).

5. Discussion

Slip distribution through a rupture area associated with a subduction zone megathrust earthquake, can be obtained by a joint inversion of different kind of data, e.g. teleseismic (P, SH and Rayleigh waves), geodetic (static and continuous GPS, Interferometry) and tsunami data. Determination of the slip distribution is influenced by the inversion method (Beresnev, 2003) and depends strongly on the type of data used for the inversion (Delouis et al., 2010). Lee et al. (2006) examined the fault geometry effect and the corresponding coseismic slip distribution for different fault models, and concluded that fault geometry also influences the results. Particularly, trial inversions (Lay et al., 2010; Shao et al., 2010) obtained for the Maule 2010 earthquake indicate that the seismic inversions are sensitive to the types of waveform data being included and the frequency band (Pollitz et al., 2011). Furthermore, in poorly resolved regions (without enough data constraints), the model would exhibit some artifacts which will look similar to seismic asperities (Page et al., 2009). Summarizing, different slip distributions can be obtained for the same seismic event, depending on the data used, the fault model geometry and the inversion method. For a detailed analysis, we superimposed the slip distribution of two of the largest earthquakes along the Chilean margin over the Tzz maps.

5.1. The Valdivia 1960 Mw = 9.5 earthquake

For this earthquake we superimposed the slip distribution of Moreno et al. (2009) over the Tzz from GOCE (Fig. 5). To obtain a variable slip distribution for this earthquake, Moreno et al. (2009) inverted the same geodetic data set as Barrientos and Ward (1990) (vertical displacement, inland elevation differences and surface shear strain compiled by Plafker and Savage, 1970). Nevertheless, instead of using an elastic dislocation model with a planar fault geometry (such as Barrientos and Ward, 1990), they implemented a precise 3D finite element model (FEM) derived from geophysical data. This model (3D FEM) avoids the occurrence of some artifacts that could be interpreted as asperities that take place when using simplified planar fault geometry. Even though the use of this model improved the final results, Moreno et al. (2009) reported that the best constrained region of the model is north of Isla de Chiloé (42°S), where most geodetical data were acquired. South of Isla de Chiloé, data used for the inversion are not as reliable as to the north.

Previous works (Wells et al., 2003) had found a coincidence between the size and distribution of coseismic slip calculated by Barrientos and Ward (1990) and the dimensions of forearc basins obtained by Mordojovich (1981) from seismic reflection surveys, which are also visible as a chain of pronounced lows in the satellite gravity data (Wells et al., 2003). They found that slip patches and basins are roughly limited by the subducted fracture zones, suggesting that the margin is seismically segmented (Barrientos and Ward, 1990).

In the Tzz map (Fig. 5), four lobes with very low gradient values are found (less than −15 Eötvös). The −10 Eötvös contour located between 38.5°S and 41.2°S coincides with the upper patch of the slip distribution. The northern lobe (−15 Eötvös), located inside this contour, coincides with the maximum slip in this area. South of Chiloé Fz (42°S to 46°S), where the slip model of Moreno et al. (2009) is not so accurate, the lobes of Tzz present a shift with respect to the peaks of the slip distribution. In Appendix D the slip distribution of Moreno et al. (2009) is superimposed to the Tzz obtained from the EGM2008 model. Here a better agreement between slip patches and low Tzz is found in most places.

5.2. The Maule 2010 Mw = 8.8 earthquake

For this event, we superimposed the models of Tong et al. (2010) (Fig. 6A), Vigny et al. (2011) (Fig. 6B) and Moreno et al. (2012) (Fig. 6C). The earthquake of Maule 2010 initiated at approximately
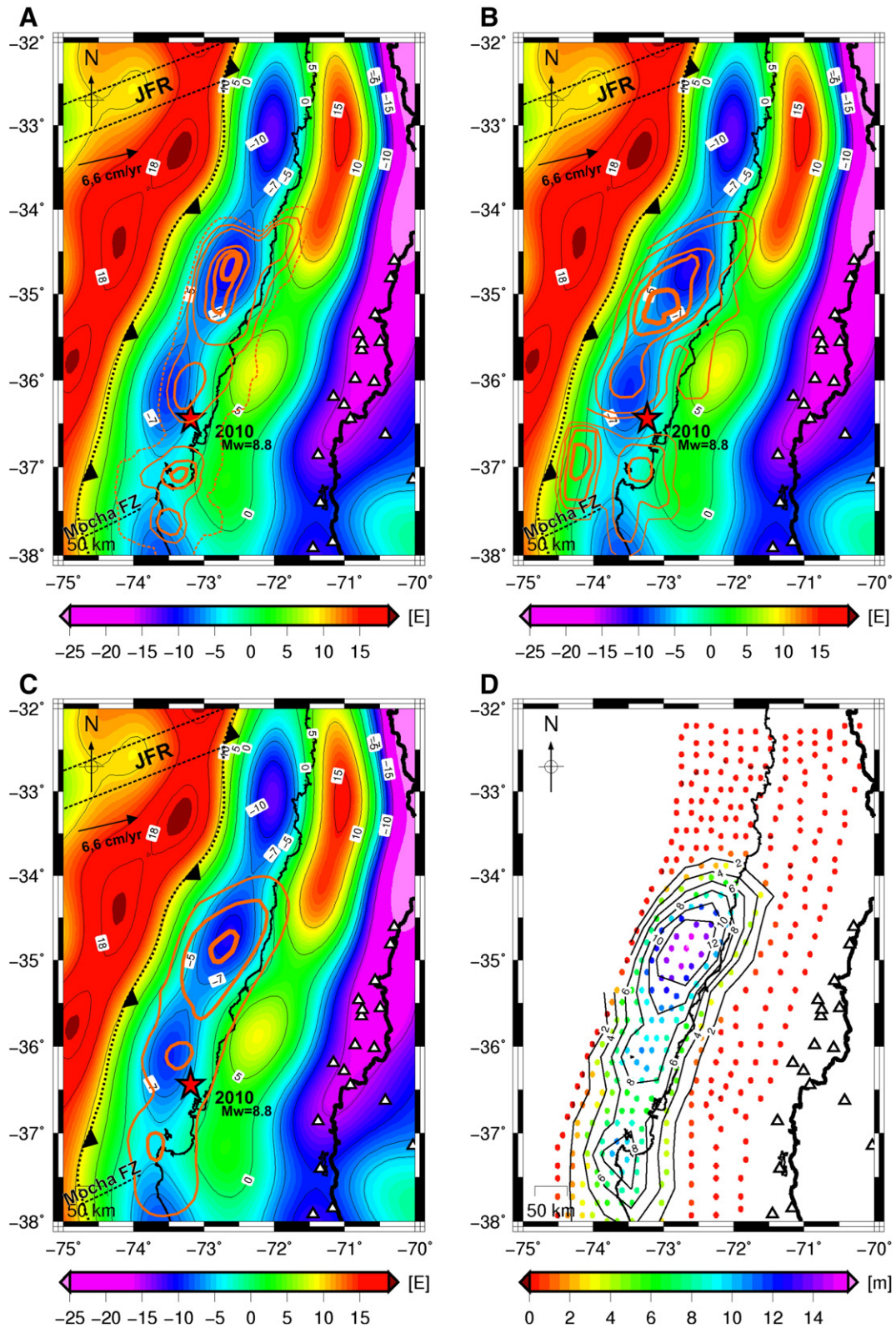
Fig. 6. GOCE vertical gravity gradient in the zone of the Maule 2010 earthquake, superimposed to fault slip distribution contours obtained by **A**: (Tong et al., 2010). B: (Vigny et al., 2011). C: (Moreno et al., 2012). Note the correlation between the northern patch for the slip models and the lobes with low Tzz values. D: Coseismic slip model for the 2010 Maule earthquake (Moreno et al. (2012).

36.5°S, and ruptured the subduction plate interface bilaterally with two major slip patches located between 34°S and 38°S (Delouis et al., 2010; Lay et al., 2010; Lorito et al., 2011; Pollitz et al., 2011; Tong et al., 2010;

among others). Different works (Table 1) show a similar spatial pattern for the Maule 2010 earthquake rupture zone. These studies roughly coincide in the location of the northern patch located approximately

Table 1
Different kind of data used in the slip models for the Maule 2010 megathrust earthquake.

Slip model	
Data used in the joint inversion model	Reference
Teleseismic (P, SH), INSAR, near and far cGPS/hrGPS	Delouis et al. (2010)
Teleseismic P, SH and Rayleigh observations	Lay et al. (2010)
Tsunami and geodetic observations (cGPS, INSAR and land-level variation from Farías et al. (2010))	Lorito et al. (2011)
INSAR, near and far cGPS	Tong et al. (2010)
INSAR, near and far cGPS and campaign GPS data	Pollitz et al. (2011)
Survey GPS, near field and far field cGPS data, land-level variation from Farías et al. (2010) and INSAR from Tong et al., 2010.	Vigny et al. (2011)
Survey GPS, continuous near field and far field GPS data, INSAR, land-level changes.	Moreno et al. (2012)

between 34°S and 36.5°S, which concentrated the major slip (15 to 20 m) between ~34.5°S and 35.5°S. Most authors, located the other patch south of the epicenter, centered at about 37°S, with a lower overall slip (less than ~10 m).

In the *Tzz* map we found two lobes (−7 Eötvös): the first located between 34°S and 35.2°S and the other between 35.5°S and 36.5°S (Fig. 6). These negative *Tzz* values show a strong correlation with the main northern slip patch of the Maule 2010 earthquake. The northern lobe

shows lower *Tzz* values in coincidence with the concentration of the major slip calculated by the different models. As an example Fig. 6 shows *Tzz* GOCE results overlapped to slip distribution models obtained by (A) Tong et al. (2010), (B) Vigny et al. (2011) and (C) Moreno et al. (2012).

Vigny et al. (2011) used data from a near-dense cGPS array constrained by land level changes from Farías et al. (2010); INSAR data from Tong et al. (2010) were only used for the areas with scarce GPS data coverage, representing only the 7% of the total dataset. Thus only in a few areas these two models included the same kind of data for the inversion, thus explaining their differences (see Fig. 6A and B). Later, Moreno et al. (2012) used a finite element model that takes into account the geometrical complexities of Chile subduction zone to avoid introducing slip artifacts due to geometrical simplification. The maximum slip for both lobes of the northern patch obtained by these authors (Fig. 6C) is better correlated with low *Tzz* lobes than the other works (Fig. 6A and B).

Even though the superposition here presented shows a general correlation between *Tzz* and slip distribution, a quantitative analysis was performed: We sampled a digital representation (Fig. 6D) of the slip model of Moreno et al. (2012, supplementary material) and the *Tzz* field over a regular grid (Fig. 7B). Then, we plotted slip vs *Tzz* (Fig. 7A) tracing a profile along *Tzz* representing also the slip distribution (Fig. 7B). The relation between high slip over negative *Tzz* is observed
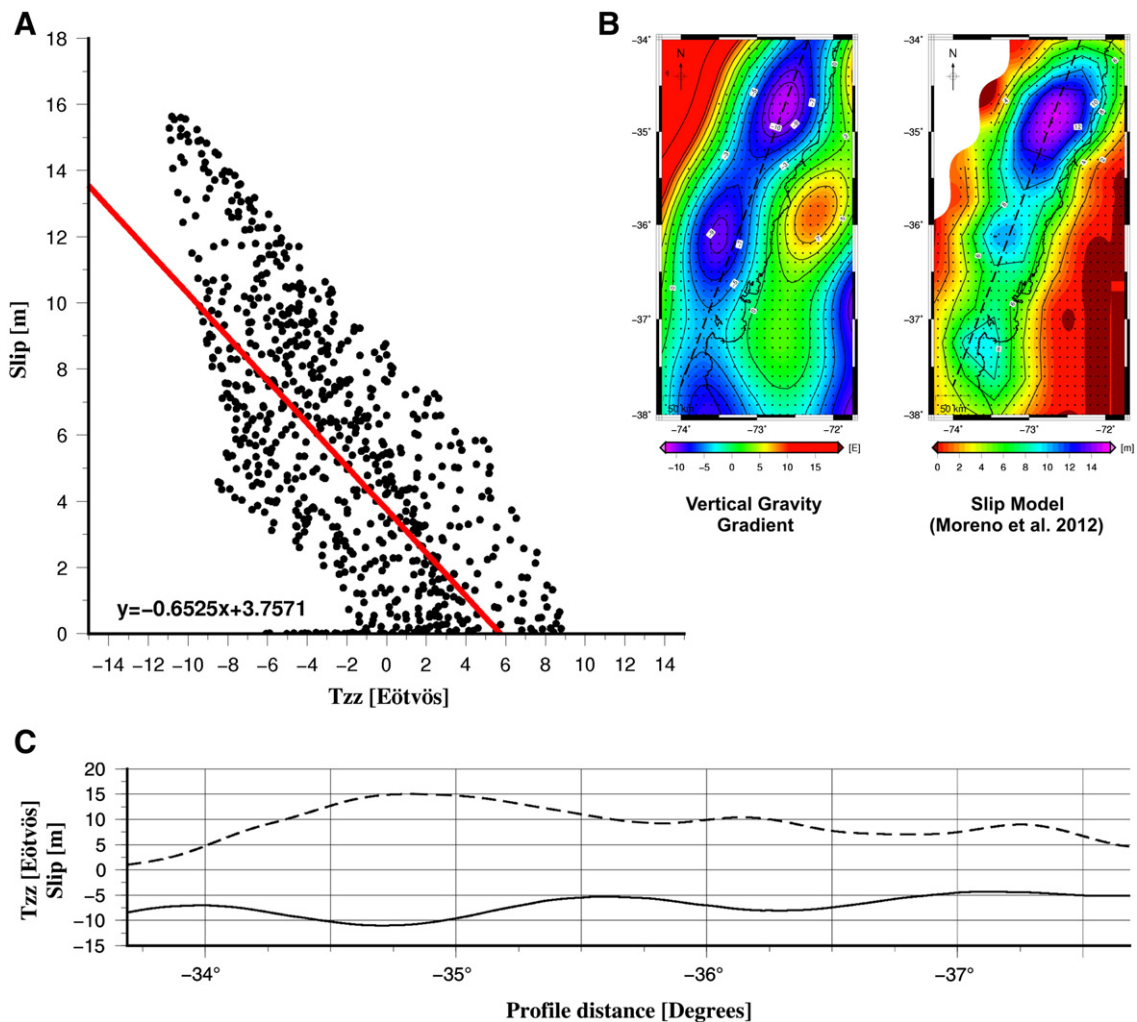

Fig. 7. A) Plot of Tzz field versus slip model both sampled over a regular grid (B) and profile along Tzz and slip distribution. In both representations an inverse relationship between both quantities is observed (high slip over negative Tzz).

in both representations. Then, we made a statistical quantification of both variables and obtained a correlation coefficient of $= -0.6919$. The deviation of data distribution regarding the fit line is $\sigma = 3.0262$ m/Eötvös. Song and Simons (2003) had proposed the premise that spatial variations in gravity over the forearc served as a proxy for the long-term state of stress on the plate interface. Wells et al. (2003) explained that the empirical relationship between large co-seismic slip and the observed gravity low along deep sea terraces and their basins may be a proxy for the long term coseismic slip distribution along some subduction zones. Since vertical gravity gradients derived from earth gravity field models present a higher resolution than gravity anomalies, this allowed us to describe this relation quantitatively and to obtain a more detailed characterization of the seismogenic structure along the Chilean subduction zone.

The southern patch, depicted by the different slip models, is not well solved by GOCE data. This may be related mainly to the fact that its size is in the order of the spatial resolution of this model. Moreover, as slip increases a better correlation with lower *Tzz* values appears, as is seen in Fig. 7A. Since the southern patch exhibits minor slip and extension than the northern patch, the correlation is weaker. When the method applied in this work, is performed using the EGM2008 model, a low *Tzz* anomaly is depicted (see Fig. B.1, Appendix B) in coincidence with the maximum slip area of the southern patch. In the Appendix A, we show a statistical analysis of the existent differences between both models defining the areas where we can be confident with the EGM2008 model. The *rms* gravity residual anomaly (Fig. A.3) shows a good agreement between both models just over the area of the Arauco peninsula, making the EGM2008 model reliable where the maximum peak of the southern patch is located. Since this high frequency anomaly is not resolved by the long wavelengths characteristic of the GOCE signal, we can infer that the southern patch is also related to low *Tzz* values.

6. Conclusions

From a direct modeling of the gravity signal using satellite GOCE data and EGM2008 model, at medium to long wavelengths, we identified an along strike segmentation of the *Tzz* signal. We showed how the different *Hof's* compartmentalize the gradient signal into well defined segments, where highs in the gradient signal appear to be related mostly to the subducted oceanic floor highs. Particularly, the *JFR*, the Mocha Fz and the Chile Rise are related to a high *Tzz* signal. We derived a spatial relation between the subduction of the *Hof's* in the oceanic lithosphere of the Nazca plate and associated segmentation of the vertical gravity gradients in the interplate zone, along the south-central Chile subduction zone. Then we compared the *Tzz* with the main and robust characteristics of the slip distribution for different megathrust earthquakes. From this, we have found a rough spatial relation between high *Tzz* values with the rupture limits for some events.

We found that low *Tzz* values are roughly correlated with the location of the rupture zones for large earthquakes along the central to southern Chile margin. In a more detailed analysis, we found a correlation between high slip and low *Tzz* values for the Maule 2010 event. The different slip models analyzed in this work exhibit some differences in relation to the kind of data and model used for the inversion. The *Tzz* presents a better adjustment with the model of Tong et al. (2010) and Moreno et al. (2012) both based on INSAR and cGPS data. This is a direct consequence of the low frequency characteristics of the GOCE signal. When the slip models are compared with *Tzz* obtained from EGM2008, a good correlation is obtained, especially for those regions where both GOCE and EGM2008 are in agreement. In this case the EGM2008 model resolves the high frequencies of the gravity gradient signal and depicts some anomalies that are not solved by GOCE. This is the case for the southern patch of the Maule 2010 earthquake.

Results suggest that *Tzz* is a better proxy than gravity anomaly to delineate along strike variable coupling of the seismogenic structure that

occurs beneath the deep-sea terrace and its basins for the analyzed segment (high coupling would be related to low *Tzz* values and lower seismic coupling to high *Tzz* values in the seismogenic zone). Since vertical gravity gradients derived from satellite models are useful for the characterization of the seismogenic structure along subduction zones, it has a number of implications on the general understanding of seismogenic processes and on seismic (and tsunami) hazard assessment.

We delineated the segmentation of the margin (Fig. 8) defining two kinds of barriers using *Tzz* contours and their relation to the large
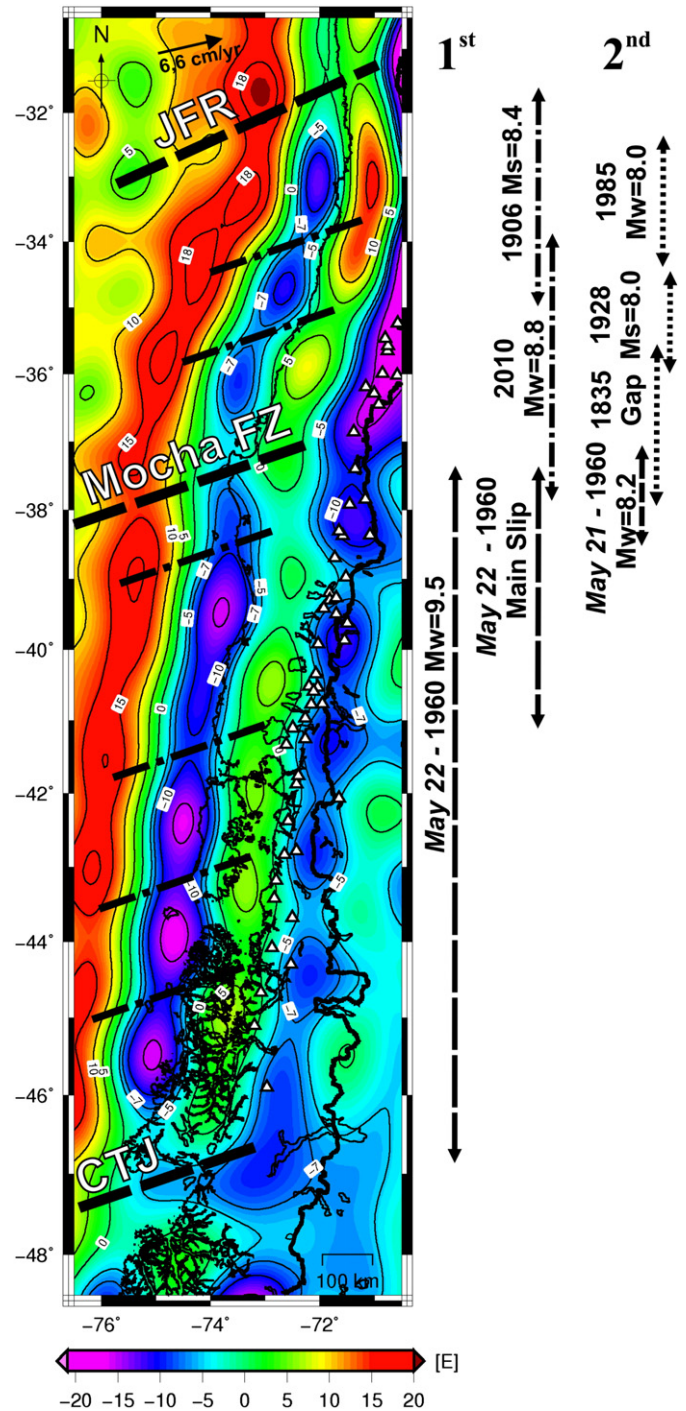

Fig. 8. Different orders of barriers/attenuators proposed that segment the southern Chilean subduction zone, based on Tzz from GOCE satellite data constrained by the available rupture zones for large megathrust earthquakes (Mw ≥ 8.0).

megathrust earthquakes in the area under study. Two main segments are distinguished, the first between *JFR* and Mocha Fz, and the second between Mocha Fz and *CTJ*. The limits of the different rupture zones are here defined as "attenuators" instead of "barriers" since these present a certain overlap (Fig. 8) and some events, particularly the 1730 earthquake (Appendix E), probably crossed these "barriers". In this sense, the vertical gravity gradient signal shows a gradual transition between highs and lows along strike (by means of the high wavelength signal of GOCE) and certain continuity in the low *Tzz* anomaly with interspersed highs along and across-strike (delineated by the high frequency EGM2008 model). The *Tzz* signal shows different higher values at the location of these "barriers", thus indicating a degree of blockage rather than a barrier to rupture propagation. We defined the *Tzz* highs related to these *Hof's* (*JFR*, Mocha Fz and *CTJ*) as first order barriers or attenuators, as they coincide with the main segmentation of the *Tzz* signal (cut off of the −5 Eötvös contour) coinciding with the limits of the two longest rupture zones occurred in this zone (Maule 2010 *Mw* = 8.8 and Valdivia 1960 *Mw* = 9.5). The second order barriers/attenuators are defined by the contours of the *Tzz* signal generating the different secondary lobes (Fig. 8).

Finally, we might conclude the following sequence of events: When a megathrust earthquake takes place, the rupture propagates along the fault interface following main asperities. Depending on its magnitude, the rupture zone would cut across these attenuators/barriers in a decreasing order until the seismic energy release would be dissipated by minor order attenuator/barrier, i.e. the main rupture zone will be restrained in function of the relation between earthquake magnitude and attenuators/barriers order.

Acknowledgments

Appendix A. GOCE vs EGM2008 data comparison

The last models available derived from data of the GOCE mission (e.g. Pail et al., 2011) have been published after more than 26 months of measurements, but with a lower spatial resolution than mixed satellite-terrestrial global models like EGM2008 (Pavlis et al., 2008). The satellite-only gravitational model of GOCE GO_CONS_GCF_2_TIM_R4, (datasheet_go_cons_gcf_2_tim_r4.pdf, http://icgem.gfz-potsdam.de/ICGEM/) is useful to examine the quality of the terrestrial data entering in the mixed satellite-terrestrial global models like EGM2008 (Pavlis et al., 2008, 2012) by a comparison analysis (see Alvarez et al., 2012; Braitenberg et al., 2011b for a more detailed description). Yi and Rummel (2014) made a comparison of GOCE models with EGM2008 and found that the agreement between EGM2008 and the GOCE-models up to degree and order 200 is good, with a global (excluding the polar gaps of GOCE orbits, throughout) geoid difference RMS of 11 cm, in the ocean areas 8 cm and 20 cm in the continental areas.

A simple way to evaluate the quality of the terrestrial data contributing to the model (for degrees greater than N = 120 EGM2008 relies entirely on terrestrial data) is to make a comparison analysis up to degree N = 250 with the pure GOCE-satellite derived model. The errors of the original terrestrial data heavily affects the errors of the EGM2008 values up to N = 250, because the spherical harmonic expansion can be seen as an averaging process. The standard deviations between GOCE and EGM2008 thus represent varying quality of the original terrestrial
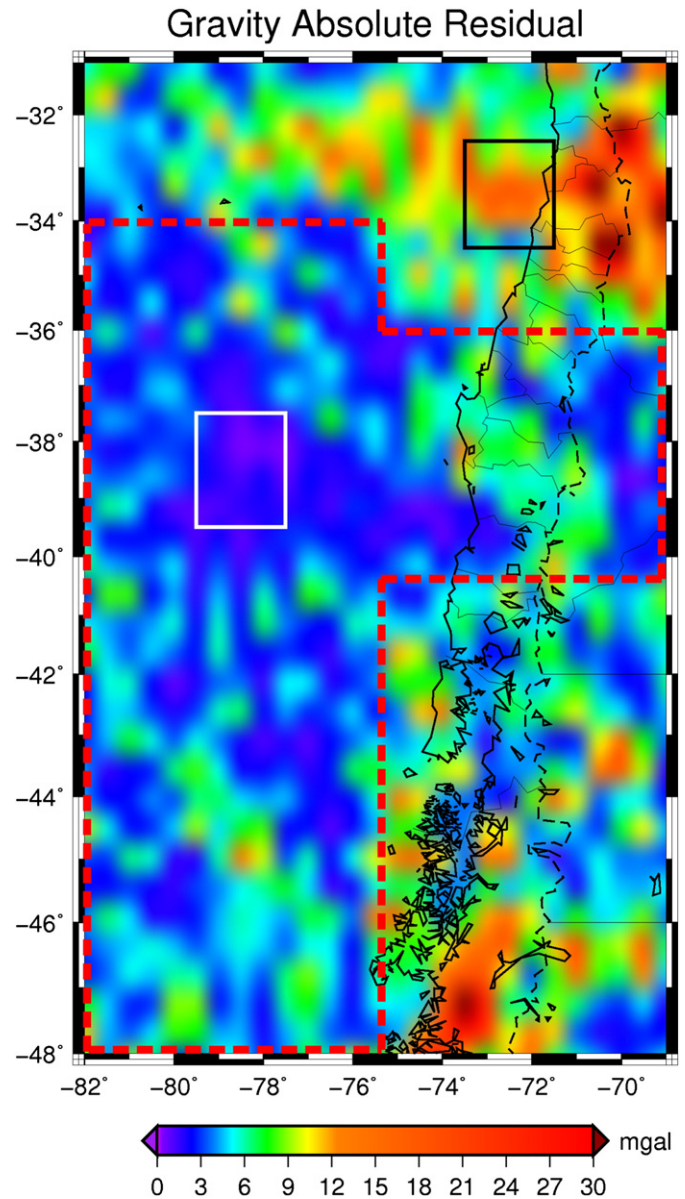

Fig. A.1. Absolute difference between the gravity anomaly from EGM08 and GOCE. The black square in the vicinity of the JFR shows an area with erroneous data. The white square shows an area over the Nazca Plate (Near Mocha FZ) with better quality data. Red dashed line indicates the most reliable areas to apply the EGM2008 model. Argentinian/Chilean border indicated by dotted and dashed line; coastal border indicated by black line.

data, because the quality of the GOCE data is locally homogeneous. Where the standard deviations are small, the original data must have been accurate or otherwise the same downscaled values and a small standard deviation would have been only obtained by chance (See Braitenberg et al. (2011a) and Alvarez et al. (2012) for a more detailed explanation). Therefore GOCE is a remarkably important independent

Table A.1
Statistical parameters for the difference.

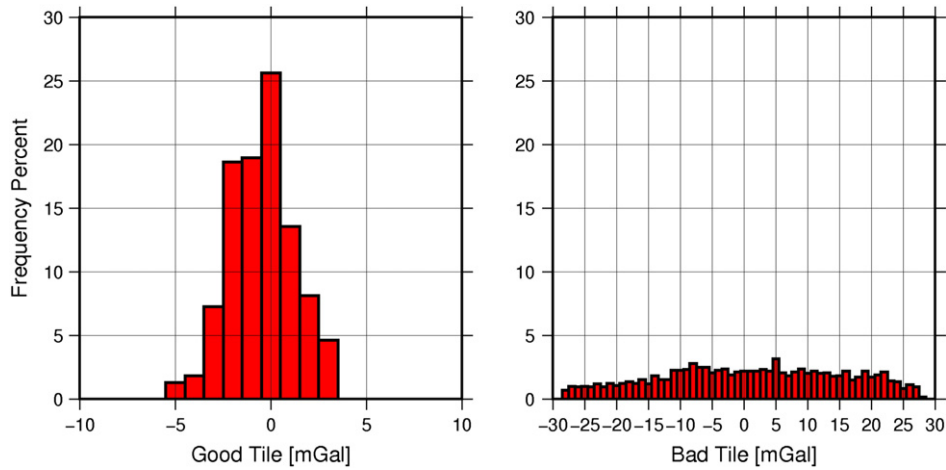|	
Average difference	0.147 mGal
Standard deviation	12.45 mGal
Maximal value of difference	52.52 mGal

Fig. A.2. Histogram of the residual gravity anomaly between EGM08 and GOCE (up to degree and order N = 250). Left (Good tile): white square of Fig. A.1. Right (Bad tile): black square of Fig. A.1.
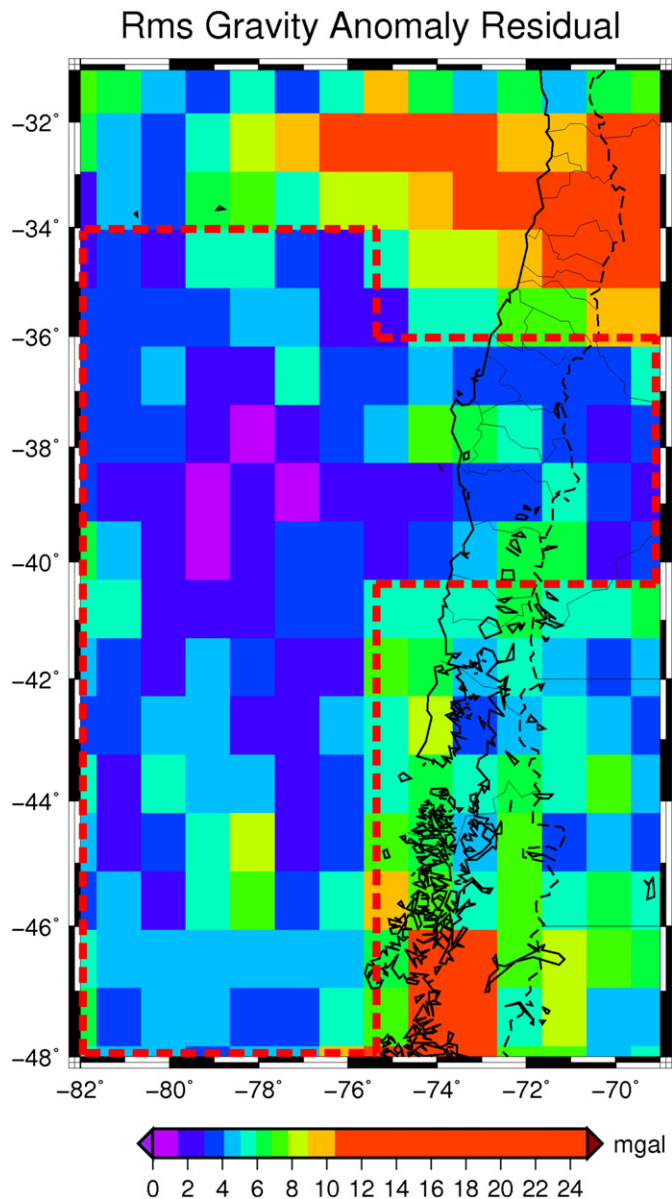

Fig. A.3. Root mean square of the gravity anomaly residual on 1 × 1 tiles. Red dashed line indicates the most reliable areas to apply the EGM2008 model.

quality assessment tool for EGM2008, especially in those areas were no precise terrestrial data are available in the EGM2008 model as is the case of large parts of South America. Here, substantial differences are expected, especially in the Andes region wherein the topography is high and very rough in many areas. An assessment for the intercomparison of terrestrial observations and EGM2008 and GOCE was made in Bomfim et al. (2013).

We calculated the gravity anomaly derived from the EGM2008 model (Pavlis et al., 2008) and from the GOCE satellite (Pail et al., 2011) up to N = 250. The absolute value of the difference field (EGM2008-GOCE) is shown in Fig. A.1. Statistical parameters for the difference between the two fields are shown on Table A.1. A high-quality region is compared with a low-quality region in terms of the residual histogram. The white square in Fig. A.2 marks a 2° × 2° area with relatively high quality; which is compared to a square of equal size (black) of degraded quality. The histograms of the residuals (Fig. A.3) illustrate a limited error ($+/-5$ *mGal*) for the white square and more than 25% of coincidence between both models (80% between $+/-2$ *mGal*). Instead, the black square, presents a high error ($+/-30$ *mGal*) with a uniform distribution.
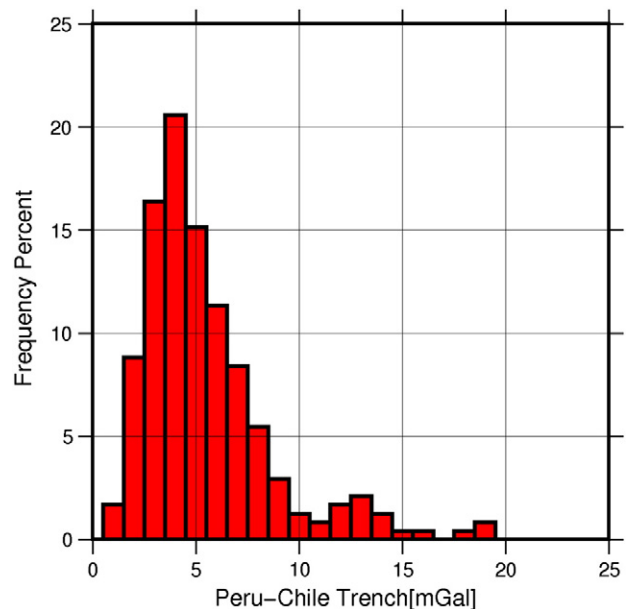

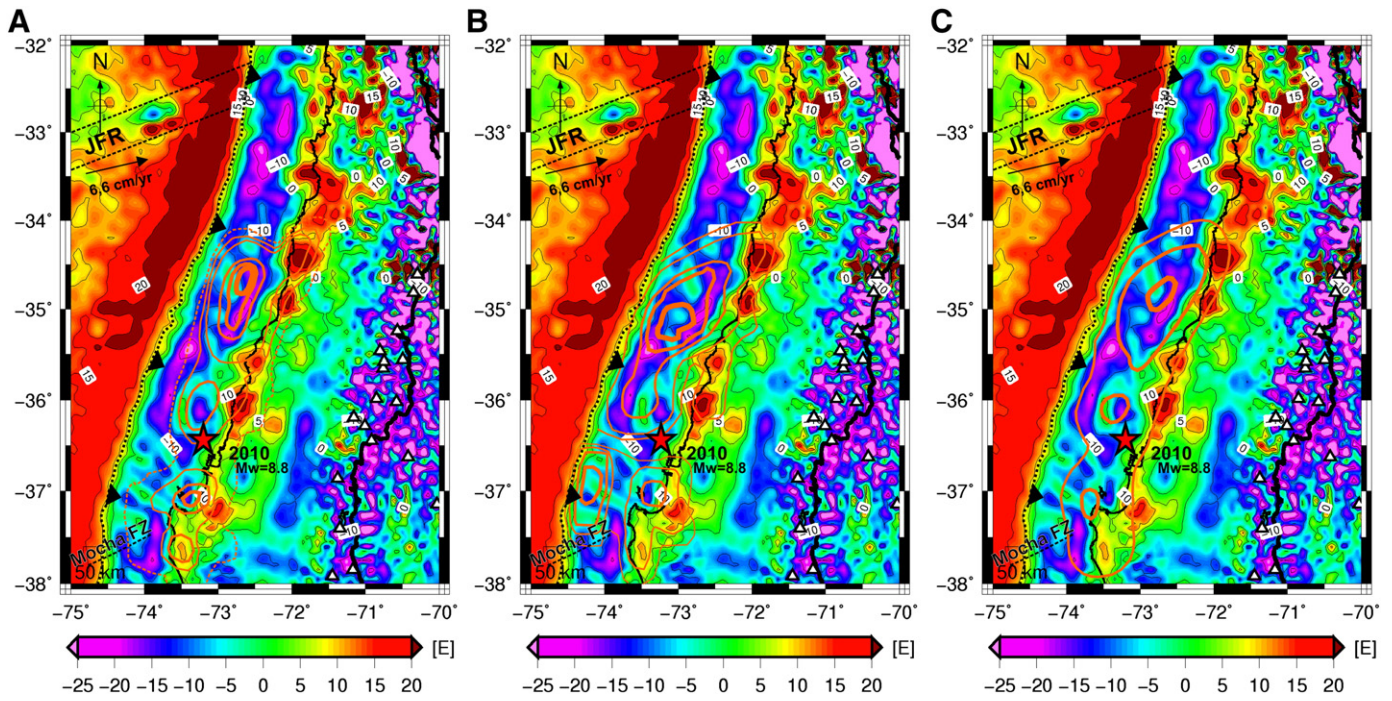**Fig. A.4.** Histogram of the rms deviations on 1 × 1 tiles.

Fig. B.1. EGM2008 Vertical Gravity Gradient in the zone of the Maule 2010 earthquake, superimposed with fault slip distribution contours obtained by the joint inversion of: A: INSAR, near and far cGPS (Tong et al., 2010). B: Survey GPS, near field and far field cGPS data, land-level variation and INSAR (Vigny et al., 2011). C: Survey and continuous near and far field GPS data, INSAR, and land-level changes (Moreno et al., 2012). Note the agreement between the maximum displacements and lower Tzz values. The maximum slip for the southern patch (at the Arauco peninsula) coincides with a low Tzz value.

The root mean square (*rms*) deviation was calculated from the mean on sliding windows of 1° × 1° as a statistical measure of EGM2008 quality. The result is shown on Fig. A.3. The most frequent value of the *rms* deviation is 4 *mGal* as is shown in Fig. A.4. The locations where the terrestrial data have problems reflected greatly increased values. The 75% of the *rms* deviation is below 6 *mGal*.

Appendix B. *Tzz* from EGM2008 model for the Maule event

Analysis made on Section 5, shows a good correspondence between the *Tzz* from GOCE and the northern patch of the slip distribution for the Maule 2010 earthquake. Nevertheless, the southern patch could not be depicted as a consequence of the high wavelength characteristic of the
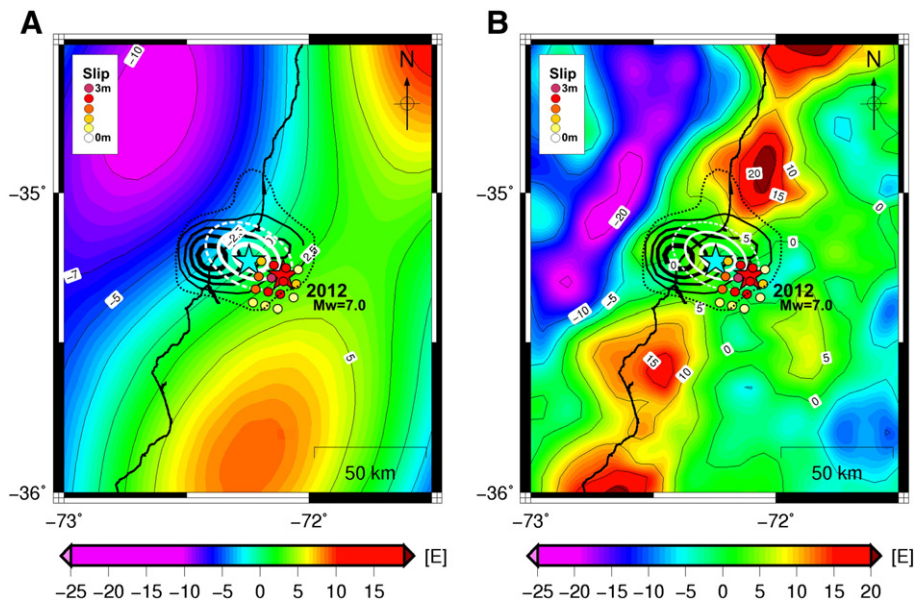

Fig. C.1. Slip model for the Constitucion 2010 Mw = 7.0 aftershock of Maule 2010 (Ruiz et al., 2013) superimposed to GOCE (A) and to EGM2008 model (B). The red and blue stars are the epicenters of the 2012 earthquake computed using the P1 and P2 waves, respectively. Slip distribution obtained from teleseismic records (color dots), together with InSAR images and GPS data (thick black line contours slip from 1 m to 0 m thin black dotted line) and from GPS and strong motion records (thick white line contours slip from 2.14 m to 0 m thin white dotted line 0 m).

GOCE signal. In this section we present the topography corrected vertical gravity gradient obtained from the EGM2008 model (Fig. B.1) superimposed with the same slip models from Fig. 6. The physiographic slope and its basins (ANCORP Working Group, 2003; Flueh et al., 1998; Von Huene et al., 1997), described by Wells et al. (2003) as a prominent
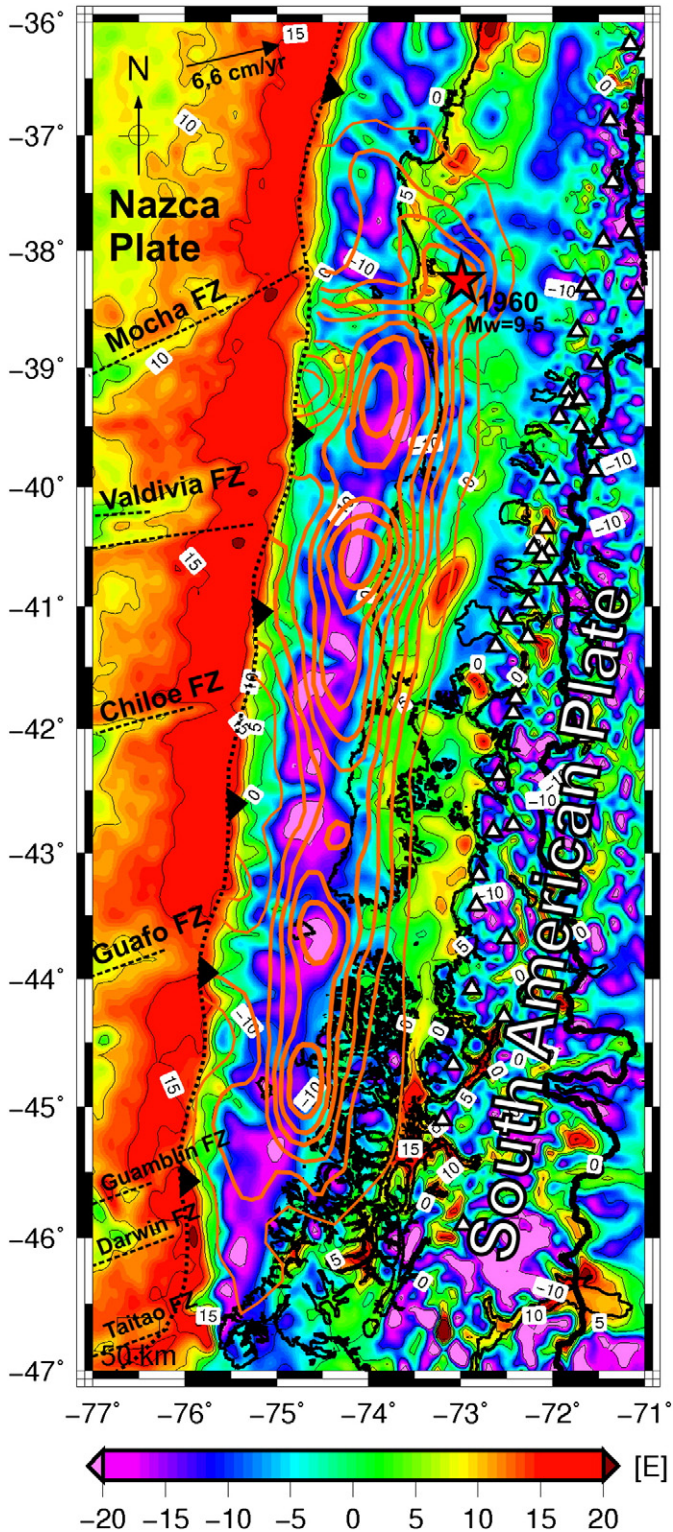

Fig. D.1. EGM2008 Vertical Gravity Gradient in the zone of the Valdivia 1960 earthquake, superimposed with fault slip distribution contours predicted by the precise 3D FEM model from Moreno et al. (2009).

free-air gravity low, are delineated with the EGM2008 model with better detail than with GOCE satellite only data.

According the prior statistical analysis, we can be confident on EGM2008 model only in a few areas over the margin. Between 36°S and 40°S the EGM2008 seems to be in good agreement with the GOCE model, especially at the Arauco peninsula. Here the *Tzz* signal shows a low value in coincidence with the peak of the slip for the southern patch depicted by the different models. The northern patch from the models of Tong et al. (2010) and Moreno et al. (2012) shows a great correspondence with low *Tzz* values. The northern patch from the Vigny et al. (2011) model, shows a N-NW orientation which coincides with the *Tzz* signal in a more regional way.

Appendix C. March 25–2012 Mw = 7.0, a Maule-2010 aftershock

One of the largest Mw = 7.0 thrust interplate aftershocks of Maule Mw = 8.8 earthquake occurred on 25 March 2012. It was recorded by a network of high-rate GPS stations, local seismometers and accelerometers, Global Seismographic network and SAR acquisitions by the ENVISAT satellite (Ruiz et al., 2013). The slip distribution of this event (Ruiz et al., 2013) is plotted in Fig. C.1 over *Tzz* from GOCE (Fig. C.1A) and over *Tzz* from EGM2008 model (Fig. C.1B). A notable concordance with lower *Tzz* values from EGM2008 and GOCE is observed, being the maximum slip between two *Tzz* highs.

Appendix D. *Tzz* from EGM2008 model for the Valdivia 1960 event

The statistical analysis (Appendix A) shows in general, a better agreement between both models south of 36°S. In Fig. D.1, we superimposed the slip model from Moreno et al. (2009) with the *Tzz* obtained from EGM2008. Here it can be noted a good correspondence, as obtained with GOCE model, but with higher resolution. By a direct comparison with Fig. 5, it can be elucidated how the GOCE signal "averages" the different anomalies, an obvious consequence of the higher spatial resolution. The size and distribution of the forearc basins (very low *Tzz*) shows a notorious coincidence with the distribution of high coseismic slip from Moreno et al. (2009) as found by Wells et al. (2003) between slip patches and basins by means of the gravity anomaly.

Appendix E. *Tzz* from GOCE and EGM2008 for the 1730 earthquake

The 1730 earthquake with an epicenter offshore near Valparaíso (33.05°S 71.63°W) and a magnitude of 8.7 affected a zone stretching for more than 1000 km along the coast from Copiapó to Concepción and caused great damage in Santiago and Valparaíso (Udias et al., 2012, 2013). Based on contemporary documents, these authors suggest that the 1730 earthquake crossed the subducted Juan Fernandez Ridge and extended from approximately 30°S to 38°S. Even though the historical record of very large earthquakes along the Nazca margin stretches back to at least 1575 (Cisternas et al., 2005), events before 1868 are insufficiently documented to determine the extent of their rupture zones in any detail (Sparkes et al., 2010). Then, we analyzed the possibility of this large rupture by means of the *Tzz*. In Fig. E.1, we plotted the *Tzz* from GOCE (A) and from EGM2008 model (B). In this figure is notorious the abrupt decrease in the negative *Tzz* anomaly over the seismogenic zone north of *JFR*. However, a negative gradient is also detected up to −29°S with GOCE and up to −28° with EGM2008 model. In this region, the agreement between both models is very poor when compared up to the same degree/order. Nonetheless, both maps are showing that exists a continuity to the north of *JFR* of the low *Tzz* values, which would indicate the possibility of a certain degree of continuity over the seismogenic zone, enabling the rupture propagation across the subducted *JFR*.
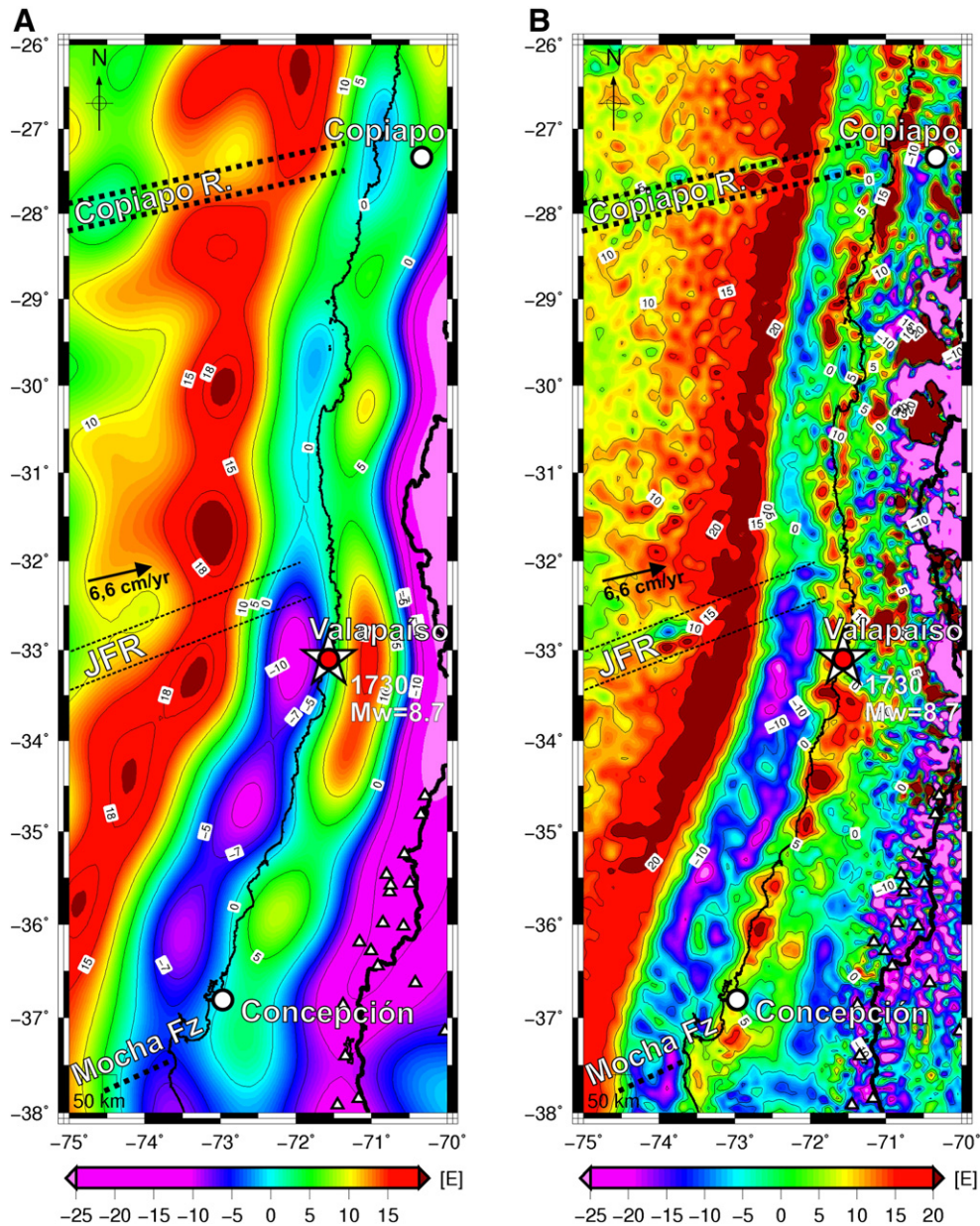
Fig. E.1. Tzz from GOCE (A) and from EGM2008 model (B) depicts important differences north of the JFR over the seismogenic zone. This reflects a decrease in sediment thickness north of JFR and no trench sediment infill at all north of Copiapo as explained by many authors (e.g. Bangs and Cande, 1997; Flueh et al., 1998; Laursen et al., 2002; Schweller et al., 1981; Völker et al., 2006; von Huene et al., 1997).

References

Alvarez, O., Gimenez, M.E., Braitenberg, C., Folguera, A., 2012. GOCE satellite derived gravity and gravity gradient corrected for topographic effect in the South Central Andes region. Geophys. J. Int. 190 (2), 941–959. http://dx.doi.org/10.1111/j.1365-246X.2012.05556.x.

Alvarez, O., Gimenez, M.E., Braitenberg, C., 2013. Nueva metodología para el cálculo del efecto topográfico para la corrección de datos satelitales. Rev. Asoc. Geol. Argent. 70 (4), 422–429.

Alvarez, O., Gimenez, M.E., Martinez, M.P., LinceKlinger, F., Braitenberg, C., 2014. New insights into the Andean crustal structure between 32° and 34°S from GOCE satellite gravity data and EGM2008 model. In: Sepúlveda, S.A., Giambiagi, L.B., Moreiras, S. M., Pinto, L., Tunik, M., Hoke, G.D., Farías, M. (Eds.), Geodynamic Processes in the Andes of Central Chile and Argentina. Geological Society, London, Special Publications, 399 (on-line fisrt. http://dx.doi.org/10.1144/SP399.3).

Amante, C., Eakins, B.W., 2009. ETOPO1 1 arc-minute global relief model: procedures, data sources and analysis. NOAA Technical Memorandum NESDIS NGDC-24, 19, March 2009.

Bangs, N.L., Cande, S.C., 1997. Episodic development of a convergent margin inferred from structures and processes along the southern Chile margin. Tectonics 16 (3), 489–505.

Barrientos, S.E., 1988. Slip distribution of the 1985 Central Chile earthquake. Tectonophysics 145 (3–4), 225–241. http://dx.doi.org/10.1016/0040-1951(88)90197-7.

Barrientos, S.E., 1995. Dual seismogenic behaviour: the 1985 central Chile earthquake. Geophys. Res. Lett. 22, 3541–3544. http://dx.doi.org/10.1029/ 95GL03316.

Barrientos, S., Ward, S., 1990. The 1960 Chile earthquake: inversion for slip distribution from surface deformation. Geophys. J. Int. 103 (3), 589–598.

Barthelmes, F., 2009. Definition of functionals of the geopotential and their calculation from spherical harmonic models. Theory and formulas used by the calculation service of the International Centre for Global Earth Models (ICGEM). Scientific Technical Report, STR09/02. GFZ German Research Centre for Geosciences, Potsdam, Germany (World Wide Web Address: http://icgem.gfz-postdam.de).

Beck, S., Barrientos, S.E., Kausel, E., Reyes, M., 1998. Source characteristics of historic earthquakes along the central Chile subduction zone. J. S. Am. Earth Sci. 11 (2), 115–129. http://dx.doi.org/10.1016/S0895-9811(98)00005-4.

Beresnev, I.A., 2003. Uncertainties in finite-fault slip inversions: to what extent to believe? (a critical review). Bull. Seismol. Soc. Am. 93, 2445–2458.

Bilek, S.L., 2007. Influence of subducting topography on earthquake rupture. In: Dixon, T., Moore, C. (Eds.), The Seismogenic Zone of Subduction Thrust Faults. Columbia University Press, pp. 123–146.

Bilek, S.L., Schwartz, S.Y., De Shon, H.R., 2003. Control of seafloor roughness on earthquake rupture behaviour. Geology 31 (5), 455–458.

Bomfim, E.P., Braitenberg, C., Molina, E.C., 2013. Mutual evaluation of global gravity models (EGM2008 and GOCE) and terrestrial data in Amazon Basin, Brazil. Geophys. J. Int. 195 (2), 870–882. http://dx.doi.org/10.1093/gji/ggt283.

Bouman, J., Ebbing, J., Fuchs, M., 2013. Reference frame transformation of satellite gravity gradients and topographic mass reduction. J. Geophys. Res. Solid Earth 118 (2), 759–774. http://dx.doi.org/10.1029/2012JB009747.

Braitenberg, C., 2014. Exploration of tectonic structures with GOCE in Africa and across-continents. Int. J. Appl. Earth Obs. Geoinf. http://dx.doi.org/10.1016/j.jag.2014.01.013 (in Press).

Braitenberg, C., Mariani, P., Ebbing, J., Sprlak, M., 2011a. The enigmatic Chad lineament revisited with global gravity and gravity-gradient fields. In: Hinsbergen, Van, et al. (Eds.), The Formation and Evolution of Africa: A Synopsis of 3.8 Ga of Earth History. Geological Society, London, Special Publications, 357, pp. 329–341.

Braitenberg, C., Mariani, P., Pivetta, T., 2011b. GOCE observations in exploration geophysics. Proceedings of '4th International GOCE User Workshop', Munich, Germany, 31 March–1 April 2011 (ESA SP-696).

Campos, J., Hatzfeld, D., Madariaga, R., Lopez, G., Kausel, E., Zollo, A., Iannacone, G., Fromm, R., Barrientos, S.E., Lyon-Caen, H., 2002. A seismological study of the 1835 seismic gap in south-central Chile. Phys. Earth Planet. In. 132, 177–195.

Cande, S.C., Leslie, R.B., Parra, J.C., Hobart, M., 1987. Interaction between the Chile ridge and the Chile trench: geophysical and geothermal evidence. J. Geophys. 92, 495–520.

Cifuentes, I.L., 1989. The 1960 Chilean earthquakes. J. Geophys. Res. 94, 665–680.

Cisternas, M., Atwater, B.F., Torrejon, F., Sawai, Y., Machuca, G., Lagos, M., Eipert, A., Youlton, C., Salgado, I., Kamataki, T., Shishikura, M., Rajendran, C.P., Malik, J.K., Rizal, Y., Husni, M., 2005. Predecessors of the giant 1960 Chile earthquake. Nature 437.

Cloos, M., 1992. Thrust-type subduction zone earthquakes and seamount asperities: a physical model for seismic rupture. Geology 20 (7), 601–604.

Cloos, M., Shreve, R.L., 1996. Shear-zone thickness and the seismicity of Chilean- and Marianas-type subduction zones. Geology 24 (2), 107–110.

Contreras-Reyes, E., Carrizo, D., 2011. Control of high oceanic features and subduction channel on earthquake ruptures along the Chile–Peru subduction zone. Phys. Earth Planet. In. 186, 49–58.

Contreras-Reyes, E., Flueh, E., Grevemeyer, L., 2010. Tectonic control on sediment accretion and subduction off south-central Chile: Implications for coseismic rupture processes of the 1960 and 2010 megathrust earthquakes. Tectonics 29, TC6018.

Darwin, C., 1840. On the connection of certain volcanic phenomena in South America; and on the formation of mountain chains and volcanoes, as the effect of the same power by which continents are elevated. Trans. Geol. Soc. Lond. Ser. 2–5, 601–631. http://dx.doi.org/10.1144/transgslb.5.3.601.

Darwin, C., 1876. Journal of Researches into the Natural History and Geology of the Countries Visited During the Voyage of the H.M.S. Beagle Round the World. John Murray, London.

Das, S., Aki, K., 1977. Fault plane with barriers: a versatile earthquake model. J. Geophys. Res. 82, 5658–5670.

Das, S., Watts, A.B., 2009. Effect of subducting seafloor topography on the rupture characteristics of great subduction zone earthquakes. In: Lallemand, S., Funicello, F. (Eds.), Subduction Zone Geodynamics. Springer-Verlag, Berlin-Heidelberg, pp. 103–118.

Delouis, B., Nocquet, J., Vallée, M., 2010. Slip distribution of the February 27, 2010 Mw = 8.8 Maule earthquake, central Chile, from static and high-rate GPS, InSAR, and broadband teleseismic data. Geophys. Res. Lett. 37. http://dx.doi.org/10.1029/2010GL043899.

DeMets, C., Gordon, R.G., Argus, D.F., 2010. Geologically current plate motions. Geophys. J. Int. 181, 1–80. http://dx.doi.org/10.1111/j.1365-246X.2009.04491.x.

Engdahl, E.R., Villasenor, A., 2002. Global Seismicity: 1900–1999. In: Lee, W.H.K., Kanamori, H., Jennings, P.C., Kisslinger, C. (Eds.), International Handbook of Earthquake and Engineering Seismology, Part A, Chapter 41. Academic Press, pp. 665–690.

Eyike, A., Werner, S.C., Ebbing, J., Dicoum, E.M., 2010. On the use of global potential field models for regional interpretation of the West and Central African Rift System. Tectonophysics 492 (1–4), 25–39. http://dx.doi.org/10.1016/j.tecto.2010.04.026.

Farías, M., Vargas, G., Tassara, A., Carretier, S., Baize, S., Melnick, D., Bataille, K., 2010. Land-level changes produced by the Mw 8.8 2010 Chilean earthquake. Science 329 (5994), 916. http://dx.doi.org/10.1126/science.1192094.

FitzRoy, R., 1839. Narrative of the surveying voyages of His Majesty's ships Adventure and Beagle between the years 1826 and 1836. Describing Their Examination of the Southern Shores of South America, and the Beagle's Circumnavigation of the GlobeHenry Colburn, London.

Floberghagen, R., Fehringer, M., Lamarre, D., Muzi, D., Frommknecht, B., Steiger, C., Piñeiro, J., da Costa, A., 2011. Mission design, operation and exploitation of the gravity field and steady-state ocean circulation explorer mission. J. Geodesy 85, 749–758.

Flueh, E.R., Vidal, N., Ranero, C.R., Hokja, A., von Huene, R., Bialas, J., Hinz, K., Cordoba, D., Danobeitia, J.J., Zelt, C., 1998. Seismic investigation of the continental margin off- and onshore Valparaiso, Chile. Tectonophysics 288, 251–263.

Franke, D., Schnabel, M., Ladage, S., Tappin, D.R., Neben, S., Djajadihardja, Y.S., Müller, C., Kopp, H., Gaedicke, C., 2008. The great Sumatra–Andaman earthquakes imaging the boundary between the ruptures of the great 2004 and 2005 earthquakes. Earth Planet. Sci. Lett. 269, 118–130.

Grombein, T., Heck, B., Seitz, K., 2010. Untersuchungen zur effizienten Berechnung topographischer Effekte auf den Gradiententensor am Fallbeispiel der Satellitengradiometriemission GOCE. KIT Scientific Reports, 7547. Karlsruhe Institute of Technology978-3-86644-510-9 1–94.

Grombein, T., Heck, B., Seitz, K., 2013. Optimized formulas for the gravitational field of a tesseroid. J. Geodesy 87, 600–645.

Hackney, R., Echtler, H.P., Franz, G., Götze, H.J., Lucassen, F., Marchenko, D., Melnick, D., Meyer, U., Schmidt, S., Tašárová, Z., Tassara, A., Wienecke, S., 2006. The segmented overriding plate and coupling at the South-Central Chilean Margin (36–42°S). In: Oncken, O., Chong, G., Franz, G., Giese, P., Götze, H.J., Ramos, V.A., Strecker, M.R., Wigger, P. (Eds.), The Andes — Active Subduction Orogeny, Frontiers in Earth Science Series. Springer-Verlag, Berlin Heidelberg New York, pp. 355–375.

Heck, B., Seitz, K., 2007. A comparison of the tesseroid, prism and point mass approaches for mass reductions in gravity field modeling. J. Geodesy 81, 121–136.

Heuret, A., Lallemand, S., Funiciello, F., Piromallo, C., Faccenna, C., 2011. Physical characteristics of subduction interface type seismogenic zones revisited. Geochem. Geophys. Geosyst. 12, Q01004. http://dx.doi.org/10.1029/2010GC003230.

Heuret, A., Conrad, C.P., Funiciello, F., Lallemand, S., Sandri, L., 2012. Relation between subduction megathrust earthquakes, trench sediment thickness and upper plate strain. Geophys. Res. Lett. 39, L05304. http://dx.doi.org/10.1029/2011GL050712.

Hirt, C., Gruber, T., Featherstone, W.E., 2011. Evaluation of the first GOCE static gravity field models using terrestrial gravity, vertical deflections and EGM2008 quasigeoid heights. J. Geodesy 85, 723–740. http://dx.doi.org/10.1007/s00190-011-0482-y.

Hirt, C., Kuhn, M., Featherstone, W.E., Göttl, F., 2012. Topographic/isostatic evaluation of new-generation GOCE gravity field models. J. Geophys. Res. 117, B05407. http://dx.doi.org/10.1029/2011JB008878.

Hofmann-Wellenhof, B., Moritz, H., 2006. Physical Geodesy, 2nd edn. Springer, Berlin (286 pp.).

Janak, J., Sprlak, M., 2006. New software for gravity field modelling using spherical armonic. Geodetic Cartogr. Horiz. 52, 1–8 (in Slovak).

Japas, M.S., Re, G.H., 2005. Geodynamic impact of arrival and subduction of oblique aseismic ridges. 6° Symposium on Andean Geodynamics (ISAG 2005, Barcelona), Extended Abstracts, pp. 408–410.

Kanamori, H., 1971. Great earthquakes at island arcs and the lithosphere. Tectonophysics 12, 187–198.

Kanamori, H., 1994. Mechanics of earthquakes. Annu. Rev. Earth Planet. Sci. 22, 207–237.

Kelleher, J.A., 1972. Rupture zones of large South American earthquakes and some predictions. J. Geophys. Res. 77, 2087–2103.

Kelleher, J., McCann, W., 1976. Buoyant zones, great earthquakes, and unstable boundaries of subduction. J. Geophys. Res. 81, 4885–4896.

Kendrick, E., Bevis, M., Smalley Jr., R., Brooks, B., Vargas, R.B., Lauría, E., Fortes, L.P.S., 2003. The Nazca — South America Euler vector and its rate of change. J. S. Am. Earth Sci. 16, 125–131.

Kodaira, S., Takahashi, N., Nakanishi, A., Miura, S., Kaneda, Y., 2000. Subducted seamount imaged in the rupture zone of the 1946 Nankaido earthquake. Science 289, 104–106.

Kopp, H., 2013. Invited review paper: the control of subduction zone structural complexity and geometry on margin segmentation and seismicity. Tectonophysics 589, 1–16. http://dx.doi.org/10.1016/j.tecto.2012.12.037.

Köther, N., Götze, H.J., Gutknecht, B.D., Jahr, T., Jentzsch, G., Lücke, O.H., Mahatsente, R., Sharm, R., Zeumann, S., 2012. The seismically active Andean and Central American margins: can satellite gravity map lithospheric structures? J. Geodyn. 59–60, 207–214. http://dx.doi.org/10.1016/j.jog.2011.11.004.

Lamb, S., Davis, P., 2003. Cenozoic climate change as a possible cause for the rise of the Andes. Nature 425, 792–797. http://dx.doi.org/10.1038/ nature02049.

Lange, D., Tilmann, F., Barrientos, S.E., Contreras-Reyes, E., Methe, P., Moreno, M., Heit, B., Agurto, H., Bernard, P., Vilotte, J.P., Beck, S., 2012. Aftershock seismicity of the 27 February 2010 Mw 8.8 Maule earthquake rupture zone. Earth Planet. Sci. Lett. 317–318, 413–425.

Laursen, J., Scholl, D.W., von Huene, R., 2002. Neotectonic deformation of the central Chile margin: deepwater forearc basin formation in response to hot spot ridge and seamount subduction. Tectonics 21 (5), 1038. http://dx.doi.org/10.1029/2001TC901023.

Lay, T., Kanamori, H., Ruff, L., 1982. The asperity model and the nature of large subduction zone earthquakes. Earthq. Prediction Res. 1, 3–71.

Lay, T., Ammon, C.J., Kanamori, H., Koper, K.D., Sufri, O., Hutko, A.R., 2010. Teleseismic inversion for rupture process of the 27 February 2010 Chile (Mw 8.8) earthquake. Geophys. Res. Lett. 37, L1330 (1. doi: I 0.1 029/201 OGL043379).

Lee, S.H., Ma, K.F., Chen, H.W., 2006. Effects of fault geometry and slip style on near-fault static displacements caused by the 1999 Chi-Chi, Taiwan earthquake. Earth Planet. Sci. Lett. 241 (1–2), 336–350.

Li, X., 2001. Vertical resolution: gravity versus vertical gravity gradient. Lead. Edge 20, 901–904.

Li, Y., Braitenberg, C., Yang, Y., 2013. Interpretation of gravity data by the continuous wavelet transform: the case of the Chad lineament (North-Central Africa). J. Appl. Geophys. 90, 62–70.

Lindquist, K., Engle, K., Stahlke, D., Price, E., 2004. Global topography and bathymetry grid improves research efforts. EOS 85 (19). http://dx.doi.org/10.1029/2004EO190003.

Llenos, A.L., Mc Guire, J.J., 2007. Influence of fore-arc structure on the extent of great subduction zone earthquakes. J. Geophys. Res. 112, B09301.

Lorito, S., Romano, F., Atzori, S., Tong, X., Avallone, A., McCloskey, J., Cocco, M., Boschi, E., Piatanesi, A., 2011. Limited overlap between the seismic gap and coseismic slip of the great 2010 Chile earthquake. Nat. Geosci. 4 (3), 173–177. http://dx.doi.org/10.1038/ngeo1073.

Mariani, P., Braitenberg, C., Ussami, N., 2013. Explaining the thick crust in Paraná basin, Brazil, with satellite GOCE gravity observations. J. S. Am. Earth Sci. 45, 209–223.

Mayer-Gürr, T., 2007. ITG-Grace03s: the latest GRACE gravity field solution computed in Bonn. Paper presented at the Joint International GSTM and SPP Symposium, 15–17 October, Potsdam, Germany.

McCann, W.R., Nishenko, S.P., Sykes, L.R., Krause, J., 1979. Seismic gaps and plate tectonics: seismic potential for major boundaries. Pure Appl. Geophys. 117 (6), 1082–1147. http://dx.doi.org/10.1007/BF00876211.

Melnick, D., Bookhagen, B., Strecker, M.R., Echtler, H.P., 2009. Segmentation of megathrust rupture zones from fore-arc deformation patterns over hundreds to millions of years, Arauco peninsula, Chile. J. Geophys. Res. 114, B01407.

Mendoza, C., Hartzell, S., Monfret, T., 1994. Wide band analysis of the 3 March 1985 central Chile earthquake: overall source process and rupture history. Bull. Seismolical Soc. Am. 84, 269–283.

Mochizuki, K., Yamada, T., Shinohara, M., Yamanaka, Y., Kanazawa, T., 2008. Weak interplate coupling by seamounts and repeating M 7 earthquakes. Science 321, 1194–1197.

Mordojovich, C., 1981. Sedimentary basins of Chilean Pacific offshore. AAPG Stud. Geol. 12, 63–82.

Moreno, M.S., Bolte, J., Klotz, J., Melnick, D., 2009. Impact of megathrust geometry on inversion of coseismic slip from geodetic data: application to the 1960 Chile earthquake. Geophys. Res. Lett. L16310 (36). http://dx.doi.org/10.1029/2009GL039276.

Moreno, M.S., Melnick, D., Rosenau, M., Baez, J., Klotz, J., Oncken, O., Tassara, A., Chen, J., Bataille, K., Bevis, M., Socquet, A., Bolte, J., Vigny, C., Brooks, B., Ryder, I., Grund, V., Smalley, B., Carrizo, D., Bartsch, M., Hase, H., 2012. Toward understanding tectonic control on the Mw 8.8 2010 Maule Chile earthquake. Earth Planet. Sci. Lett. 321–322, 152–165. http://dx.doi.org/10.1016/j.epsl.2012.01.006.

Müller, R.D., Landgrebe, T.C.W., 2012. The link between great earthquakes and the subduction of oceanic fracture zones. Solid Earth 3, 447–465. http://dx.doi.org/10.5194/se-3-447-2012.

Page, M.T., Custódio, S., Archuleta, R.J., Carlson, J.M., 2009. Constraining earthquake source inversions with GPS data: 1. Resolution-based removal of artifacts. J. Geophys. Res. 114, B01314. http://dx.doi.org/10.1029/2007JB005449.

Pail, R., Bruisma, S., Migliaccio, F., Förste, C., Goiginger, H., Schuh, W.D., Höck, E., Reguzzoni, M., Brockmann, J.M., Abrikosov, O., Veichers, M., Fecher, T., Mayrhofer, R., Krasbutter, I., Sansò, F., Tscherning, C.C., 2011. First GOCE gravity field models derived by three different approaches. J. Geodesy 85, 819–843.

Pavlis, N.K., Holmes, S.A., Kenyon, S.C., Factor, J.K., 2008. An earth gravitational model to degree 2160: EGM2008. Paper Presented at the 2008 General Assembly of the European Geosciences Union, Vienna, Austria.

Pavlis, N.K., Holmes, S.A., Kenyon, S.C., Factor, J.K., 2012. The development and evaluation of the Earth Gravitational Model 2008. J. Geophys. Res. 117, B04406.

Plafker, G., Savage, J.C., 1970. Mechanism of the Chilean earthquake of May 21 and 22, 1960. Geol. Soc. Am. Bull. 81, 1001–1030.

Pollitz, F.F., Brooks, B., Tong, X., Bevis, M.G., Foster, J.H., Bürgmann, R., Smalley, R.J., Vigny, C., Socquet, A., Ruegg, J.C., Campos, J., Barrientos, S., Parra, H., Baez Soto, J.C., Cimbaro, S., Blanco, M., 2011. Coseismic slip distribution of the February 27, 2010 Mw 8.8 Maule, Chile earthquake. Geophys. Res. Lett. 38 (L09309). http://dx.doi.org/10.1029/2011GL047065.

Ranero, C., von Huene, R., Weinrebe, W., Reichert, C., 2006. Tectonic processes along the Chile convergent margin. In: Oncken, et al. (Eds.), The Andes-Active Subduction Orogeny, Frontiers in Earth Science Series. Springer-Verlag, New York, pp. 91–121.

Reguzzoni, M., Sampietro, D., 2010. An inverse gravimetric problem with GOCE data. International Association of Geodesy Symposia. Gravity, Geoid and Earth Observation, 135 (5). Springer-Verlag, pp. 451–456. http://dx.doi.org/10.1007/978-3-642-10634-7_60.

Robinson, D.P., 2007. Identification of Geological Features Controlling the Earthquake Rupture Process from Analysis of Broadband Seismograms. Ph.D. Department of Earth Sciences, University of Oxford, Oxford (145 pp.).

Ruegg, J., Rudloff, A., Vigny, C., Madariaga, R., de Chabalier, J.B., Campos, J., Kausel, E., Barrientos, S., Dimitrov, D., 2009. Interseismic strain accumulation measured by GPS in the seismic gap between Constitución and Concepción in Chile. Phys. Earth Planet. Inter. 175 (1–2), 78–85. http://dx.doi.org/10.1016/j.pepi.2008.02.015.

Ruff, L.J., 1989. Do trench sediments affect great earthquake occurrence in subduction zones? Pure Appl. Geophys. 129, 263–282.

Ruff, L.J., 1996. Seamounts make earthquakes. Nature 381, 371–372. http://dx.doi.org/10.1038/381371a0.

Ruff, L.J., Kanamori, H., 1980. Seismicity and the subduction process. Phys. Earth Planet. Inter. 23, 240–252.

Ruiz, S., Madariaga, R., Astroza, M., Saragoni, G.R., Lancieri, M., Vigny, C., Campos, J., 2012. Short period rupture process of the 2010 Mw8.8 Maule earthquake in Chile. Earthq. Spectra 28 (S1), S1–S18.

Ruiz, S., Grandin, R., Dionicio, V., Satriano, C., Fuenzalida, A., Vignyc, C., Kiraly, E., Meyer, C., Baez, J.C., Riquelme, S., Madariaga, R., Campos, J., 2013. The Constitución earthquake of 25 March 2012: a large aftershock of the Maule earthquake near the bottom of the seismogenic zone. Earth Planet. Sci. Lett. 377–378, 347–357.

Rummel, R., Yi, W., Stummer, C., 2011. GOCE gravitational gradiometry. J. Geodesy 85 (11), 777–790. http://dx.doi.org/10.1007/s00190-011-0500-0 (2011.33).

Schertwath, M., Contreras-Reyes, E., Flueh, E., Grevemeyer, I., Krabbenhoeft, A., Papenberg, C., Petersen, C., Weinrebe, R.W., 2009. Deep lithospheric structures along the southern central Chile margin from wide-angle P-wave modelling. Geophys. J. Int. 179 (1), 579–600.

Scholl, D., Huene, R., Kirby, S., 2010. The Aleutian Alaska subduction zone is prone to rupture in great and giant megathrust earthquakes—how scientific information can mitigate consequences. Newsletter of the Alaska Geological SocietyBP Energy Center (September 2010).

Scholz, C.H., Small, C., 1997. The effect of seamount subduction on seismic coupling. Geology 25 (6), 487–490.

Schweller, W.J., Kulm, L.D., Prince, R.A., 1981. Tectonics structure, and sedimentary framework of the Perú-Chile Trench. In: Kulm, L.D., et al. (Eds.), Nazca Plate: Crustal formation and Andean convergence. Memoirs of the Geological Society of America, 154, pp. 23–349.

Shao, G., Li, X., Liu, Q., Zhao, X., Yano, T., Ji, C., 2010. Preliminary slip model of the Feb 27, 2010 Mw = 8.9 Maule, Chile Earthquake. http://www.geol.uvsb.edu/faculty/ji/big_earthquakes/2010/02/27/chile_2_27.html.

Siebert, L., Simkin, T., 2002. Volcanoes of the world: an illustrated catalog of Holocene volcanoes and their eruptions. Smithsonian Institution, Global Volcanism Program

Digital Information Series, GVP-3 (World Wide Web Address: http://www.volcano.si.edu/world/).

Singh, S.C., Hananto, N., Mukti, M., Robinson, D.P., Das, S., Chauhan, A., Carton, H., Gratacos, B., Midnet, S., Djajadihardja, Y., 2011. Aseismic zone and earthquake segmentation associated with a deep subducted seamount in Sumatra. Nat. Geosci. 4, 308–311.

Sobiesiak, M.M., Meyer, U., Schmidt, S., Götze, H.J., Krawczyk, C., 2007. Asperity generating upper crustal sources revealed by b-value and isostatic residual anomaly grids in the area of Antofagasta. J. Geophys. Res. 112, B12308. http://dx.doi.org/10.1029/2006JB004796.

Song, T.R., Simons, M., 2003. Large trench-parallel gravity variations predict seismogenic behavior in subduction zones. Science 301, 630–633.

Sparkes, R., Tilmann, F., Hovius, N., Hillier, J., 2010. Subducted seafloor relief stops rupture in South American great earthquakes: implications for rupture behaviour in the 2010 Maule, Chile earthquake. Earth Planet. Sci. Lett. 298, 89–94. http://dx.doi.org/10.1016/j.epsl.2010.07.029.

Stummer, C., Siemes, C., Pail, R., Frommknecht, B., Floberghagen, R., 2012. Upgrade of the GOCE level 1b gradiometer processor. Adv. Space Res. 49 (4), 739–752. http://dx.doi.org/10.1016/j.asr.2011.11.027.

Tassara, A., 2010. Control of forearc density structure on megathrust shear strength along the Chilean subduction zone. Tectonophysics 495, 34–47. http://dx.doi.org/10.1016/j.tecto.2010.06.004.

Tong, X., Sandwell, D., Luttrell, K., Brooks, B., Bevis, M., Shimada, M., Foster, J., Smalley Jr., R., Parra, H., Soto, J.C.B., Blanco, M., Kendrick, E., Genrich, J., Caccamise II, D.J., 2010. The 2010 Maule, Chile earthquake: downdip rupture limit revealed by space geodesy. Geophys. Res. Lett. 37. http://dx.doi.org/10.1029/2010GL045805.

Tscherning, C.C., 1976. Computation of the second-order derivatives of the normal potential based on the representation by a Legendre series. Manuscripta Geod. 1 (1), 71–92.

Udias, A., Madariaga, R., Buforn, E., Muñoz, D., Ros, M., 2012. The large Chilean historical earthquakes of 1647, 1657, 1730, and 1751 from contemporary documents. Bull. Seismol. Soc. Am. 102 (4), 1639–1653. http://dx.doi.org/10.1785/0120110289.

Udias, A., Buforn, E., Madariaga, R., 2013. Large Chilean earthquakes and tsunamis of 1730 and 1751: new analysis of historical data. EGU General Assembly. Geophys. Res. Abstr. 15 (EGU2013-1079).

Uieda, L., Ussami, N., Braitenberg, C.F., 2010. Computation of the gravity gradient tensor due to topographic masses using tesseroids. Eos. Trans. AGU 91 (26) (Meeting America Supply, Abstract G22A-04. World Wide Web Address: http://code.google.com/p/tesseroids/).

Uyeda, S., Kanamory, H., 1979. Back-arc opening and the mode of subduction. J. Geophys. Res. 84, 1049–1061.

Vigny, C., Socquet, A., Peyrat, S., Ruegg, J.C., Métois, M., Madariaga, R., Morvan, S., Lancieri, M., Lacassin, R., Campos, J., Carrizo, D., Bejar-Pizarro, M., Barrientos, S., Armijo, R., Aranda, C., Valderas-Bermejo, M.-C., Ortega, I., Bondoux, F., Baize, S., Lyon-Caen, H., Pavez, A., Vilotte, J.P., Bevis, M., Brooks, B., Smalley, R., Parra, H., Baez, J.-C., Blanco, M., Cimbaro, S., Kendrick, E., 2011. The 2010 Mw 8.8 Maule megathrust earthquake of Central Chile, monitored by GPS. Science 332 (6036), 1417–1421. http://dx.doi.org/10.1126/science.1204132.

Völker, D., Wiedicke, M., Ladage, S., Gaedicke, C., Reichert, C., Rauch, K., Kramer, W., Heubeck, C., 2006. Latitudinal variation in sedimentary processes in the Peru–Chile trench off Central Chile. In: Oncken, et al. (Eds.), The Andes- Active Subduction Orogeny. Frontiers in Earth Science Series, Part II. Springer-Verlag, Berlin Heidelberg New York, pp. 193–216.

von Huene, R., Corvalán, J., Flueh, E.R., Hinz, K., Korstgard, J., Ranero, C.R., Weinrebe, W., CONDOR scientists, 1997. Tectonic control of the subducting Juan Fernández Ridge on the Andean margin near Valparaiso, Chile. Tectonics 16 (3), 474–488.

Wang, K., Bilek, S., 2011. Do subducting seamounts generate or stop large earthquakes? Geology 39, 819–822. http://dx.doi.org/10.1130/G31856.1.

Watts, A.B., Koppers, A.A.P., Robinson, D.P., 2010. Seamount subduction and earthquakes. Oceanography 23 (1), 166–173.

Wells, R.E., Blakely, R.J., Sugiyama, Y., Scholl, D.W., Dinterman, P.A., 2003. Basin centered asperities in great subduction zone earthquakes: a link between slip, subsidence and subduction erosion? J. Geophys. Res. 108 (B10), 2507–2536. http://dx.doi.org/10.1029/2002JB002072.

Wessel, P., Smith, W.H.F., 1998. New, improved version of the generic mapping tools released. Eos. Trans. AGU 79 (47), 579.

Whittaker, J., Goncharov, A., Williams, S., Müller, R.D., Leitchenkov, G., 2013. Global sediment thickness data set updated for the Australian–Antarctic Southern Ocean. Geochem. Geophys. Geosyst. 14, 3297–3305. http://dx.doi.org/10.1002/ggge.20181.

Wild-Pfeiffer, F., 2008. A comparison of different mass element for use in gravity gradiometry. J. Geodesy 82, 637–653.

ANCORP Working Group, 2003. Seismic imaging of a convergent continental margin and plateau in the central Andes (Andean Continental Research Project 1996 (ANCORP'96)). J. Geophys. Res. 108 (B7), 2328. http://dx.doi.org/10.1029/2002JB001771.

Yáñez, G.A., Ranero, C.R., von Huene, R., Díaz, J., 2001. Magnetic anomaly interpretation across the southern central Andes (32°S–34°S): the role of the Juan Fernandez Ridge in the late Tertiary evolution of the margin. J. Geophys. Res. 106 (B4), 6,325–6,345.

Yi, W., Rummel, R., 2014. A comparison of GOCE gravitational models with EGM2008. J. Geodyn. 73, 14–22. http://dx.doi.org/10.1016/j.jog.2013.10.004.